JM PAPERS

On Richtmyer–Meshkov finger collisions in a light fluid layer under reshock conditions

Xu Guo[1], Zhouyang Cong[1], Ting Si[1],† and Xisheng Luo[1,2]

[1]Advanced Propulsion Laboratory, Department of Modern Mechanics, University of Science and Technology of China, Hefei 230026, PR China

[2]State Key Laboratory of High Temperature Gas Dynamics, Institute of Mechanics, Chinese Academy of Sciences, Beijing 100190, PR China

The fingers known as bubbles (spikes) resulting from the penetration of light (heavy) fluids into heavy (light) fluids are significant large-scale features of Richtmyer–Meshkov instability (RMI). Through shock-tube experiments, we study finger collisions in light fluid layers under reshock conditions. Four unperturbed fluid layers with varying thicknesses are created to analyse the motion of waves and interfaces during finger collisions. The wave dynamics, sensitive to initial layer thicknesses, are characterized by a one-dimensional theory. Eight perturbed fluid layers, with four thicknesses and two interface phase combinations, are generated to explore the finger collision mechanism. It is shown that after reshock, the initial in-phase and anti-phase cases undergo spike–bubble rear-end collisions (SBCs) and spike–spike head-on collisions (SSCs), respectively. Compared with SBCs, SSCs significantly suppress spike growth, leading to the attenuation of perturbation growth, especially for larger thicknesses. As the initial thickness decreases, an SSC impedes the downstream interface from reversing its phase, resulting in abnormal RMI, thereby reducing the SSC's effectiveness in attenuating growth. The effects of rarefaction waves enhance both interfaces' amplitudes and the whole layer's thickness, diminishing the intensity of finger collisions, while the second reshock exerts an opposing influence. Linear and nonlinear models, incorporating the influence of reshocks and rarefaction waves, are developed to predict the interface perturbation growth before and after finger collisions.

Key words: shock waves

1. Introduction

Richtmyer–Meshkov instability (RMI) occurs at a perturbed density interface subjected to an impulsive acceleration, typically induced by a shock wave (Richtmyer 1960;

† Email address for correspondence: tsi@ustc.edu.cn

Meshkov 1969). Generally, the growth of perturbations at the interface initially enters a linear period and then a nonlinear period, characterized by large-scale interpenetrating finger structures of bubbles (light fluids protruding into heavy ones) and spikes (heavy fluids protruding into light ones). At late times, transition might be achieved, leading to a turbulent flow. The RMI is closely related to the well-known Rayleigh–Taylor instability (RTI) (Rayleigh 1883; Taylor 1950), a phenomenon that occurs when light fluids continually accelerate heavy fluids. Thus RMI can be regarded as the impulsive counterpart of RTI. In past decades, RMI has received extensive attention due to its essential role in basic science research and engineering applications, such as supernova explosions (Kuranz *et al.* 2018), scram-jet engines (Urzay 2018) and inertial confinement fusion (ICF) (Betti & Hurricane 2016). In RMI, the interpenetration of fingers causes pronounced deformation of the developing interface, driving perturbation growth and mixing (Sadler *et al.* 2024). In particular, in ICF, bubbles distort the ablation front while spikes introduce the cold fuel into the hotspot, giving rise to mixing between the outer ablator and inner fuels (Cheng *et al.* 2015; Clark *et al.* 2017; Mikaelian & Olson 2020). This diminishes the purity of fusion fuel, resulting in a reduction or even elimination of the thermonuclear yield (Lindl *et al.* 2014; Pak *et al.* 2020). Most previous studies, involving theoretical modelling (Goncharov 2002; Zhang & Guo 2016, 2022; Liu, Zhang & Xiao 2023), experiments (Sadot *et al.* 1998; Collins & Jacobs 2002; Mariani *et al.* 2008; Mansoor *et al.* 2020) and numerical simulations (Dimonte & Ramaprabhu 2010; Buttler *et al.* 2012; Bai, Deng & Jiang 2018; Probyn *et al.* 2021), have focused on finger development in RMI at a single interface (Zhou 2017*a*,*b*; Zhou *et al.* 2019, 2021). Nevertheless, RMI often occurs at finite-thickness fluid layers (Liang & Luo 2023*b*), such as those in ICF capsules and supernovae. In these scenarios, the evolving fingers at adjacent interfaces might contact, leading to finger collisions. These collisions can hinder finger development, contributing to the suppression of perturbation growth in ICF. As a result, it is of significance to investigate the finger collisions at a finite-thickness fluid layer.

Studies on the instability development of fluid layers have been carried out extensively. Theoretically, Taylor (1950) was the first to explore fluid-layer perturbation growth in RTI. It was found that the coupling effect between the two interfaces becomes pronounced when the layer thickness is below one-third of the wavelength. Mikaelian (1995, 1996) extended the study to fluid layers in RMI. By defining a coupling angle to characterize the interface coupling strength, Mikaelian (1995, 1996) proposed a model to describe the linear growth rates of both interfaces. Jacobs *et al.* (1995) established an alternative linear model for predicting the layer perturbation growth by solving velocity potential functions. Recently, the model of Jacobs *et al.* (1995) has been extended to a fluid layer separating three different fluids (Liang & Luo 2022*a*). These theories have shown strong capabilities in describing the amplitude growth of fluid layers prior to the collision of the two interfaces (Zhou 2017*a*,*b*; Liang & Luo 2023*b*).

The first gas-layer experiment was conducted by Jacobs *et al.* (1993), who created a vertically flowing curtain of SF_6 in a horizontal shock tube. Later, Balakumar *et al.* (2008*a*,*b*) enhanced the membraneless interface formation technique of Jacobs *et al.* (1993) and generated a perturbed heavy gas layer with improved repeatability. Using this layer type, studies have explored the dependence of late-time mixing on incident Mach numbers and initial shapes (Orlicz *et al.* 2009, 2015; Balasubramanian, Orlicz & Prestridge 2013; Orlicz, Balasubramanian & Prestridge 2013), while finger collisions have received limited attention. Recently, a membraneless gas layer with a flat interface on top and a single-mode interface below was generated in a vertical shock tube using two different combinations of three gases: air over CO_2 over SF_6, and helium over air over SF_6 (Schalles *et al.* 2024). It was shown that the existence of the upper, initially flat interface reduces the

nonlinear amplitude growth compared with an equivalent single interface configuration. However, this flat interface configuration is unfavourable for studying finger collisions.

The soap-film technique (Liu *et al.* 2018; Li *et al.* 2023) has been used to generate fluid layers. This interface formation technique provides a suitable experimental condition for studying finger collisions, since it ensures the controllability of initial layer configurations, including interface amplitudes and phases, and layer thicknesses, as well as density combinations. Using the soap-film technique, Liang & Luo (2021, 2022*a*,*b*, 2023*a*) formed various fluid layers, and examined the influence of interface coupling and reverberating waves on the amplitude growth of both perturbations. These studies have focused primarily on the regime before the two interfaces contact, while the instability development after finger collisions remains unclear, motivating the current work.

Previous shock-tube studies (Liang & Luo 2023*b*) have demonstrated that under the impact of a single shock, the fingers of the layer evolve slowly so that the collisions between fingers are not significant. In this work, a reshock that propagates in the opposite direction to the incident shock is considered. The reshock would inject energy into the developing interface, accelerating the evolution of fingers and thus intensifying their collisions. Additionally, after the reshock impact, the interface's velocity would be significantly reduced (Brouillette & Sturtevant 1993), causing the mixing layer to almost evolve at a fixed position. This is advantageous for the observation of finger collisions in shock-tube experiments. Note that reshock is common in practical situations (Zhou 2017*a*,*b*), such as in ICF, where reshock is generated due to the reflection of the incident shock after reaching the capsule centre (Lindl *et al.* 2014). The reshock would return to impact the developing material layer, markedly influencing the finger development (Balakumar *et al.* 2008*b*; Balasubramanian *et al.* 2012; Mohaghar *et al.* 2017, 2019). Thus exploring finger collisions under reshock conditions is also significant.

In this work, shock-tube experiments are conducted to study finger collisions in a light fluid layer under reshock conditions. The light fluid layer is closely associated with double-shell ICF implosion, wherein a lower-density foam is employed as the cushion between the higher-density outer and inner shells (Montgomery *et al.* 2018). Unlike other layer types where wave-induced Rayleigh–Taylor effects are evident (Liang & Luo 2021, 2022*a*, 2023*a*), the light layer case involves only RMI before reshock (Liang & Luo 2022*b*), thereby eliminating the potential impact of Rayleigh–Taylor effects on finger collisions after reshock. The soap-film technique is utilized to generate the SF_6/air/SF_6 light layers. The research content of this paper is outlined as follows. First, to understand the wave dynamics and interface motions during finger collisions, unperturbed light layer experiments and one-dimensional (1-D) theoretical analyses are performed. Then eight distinct perturbed layer cases, with four thicknesses and two interface phase combinations, are examined to explore the finger collision mechanism as well as the dependence of collisions on initial conditions. Finally, linear and nonlinear models are developed to quantify the perturbation growth for both interfaces before and after collisions.

2. Experimental set-up and methods

Figure 1 shows the initial configurations of the perturbed light fluid layers. Two sinusoidal interfaces with in-phase or anti-phase configurations, as presented in figures 1(*a*,*b*), are positioned at both sides of the fluid layer to create different types of finger collisions. For the convenience of labelling and discussion, the upstream interface of the layer is designated as interface 1 (I1), while the downstream interface is designated as interface 2 (I2). In the Cartesian coordinate system, the perturbations at I1 and I2 can be
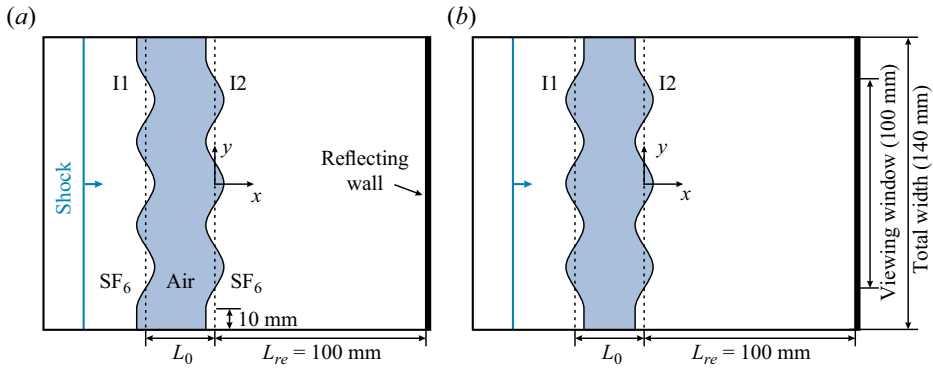
Figure 1. Initial arrangements of the light fluid layer for the perturbed case with (*a*) in-phase and (*b*) anti-phase configurations. Here, I1 and I2 denote the upstream and downstream interfaces, respectively; L_0 and L_{re} denote the initial fluid-layer thickness and the reflection distance, respectively.

Case	L50-IP	L30-IP	L10-IP	L5-IP	L50-AP	L30-AP	L10-AP	L5-AP
L_0 (mm)	50	30	10	5	50	30	10	5
a_0^{I1} (mm)	2	2	2	2	−2	−2	−2	−2
a_0^{I2} (mm)	2	2	2	2	2	2	2	2

Table 1. Initial parameters of the perturbed fluid-layer cases. L_0, the initial fluid-layer thickness; a_0^{I1} and a_0^{I2}, the initial amplitudes of I1 and I2.

expressed as $-L_0 + x = a_0^{I1} \cos(ky)$ and $x = a_0^{I2} \cos(ky)$. Here, a_0^{I1} and a_0^{I2} denote the initial amplitudes of I1 and I2, k ($= 2\pi/\lambda$, with λ the initial interface wavelength 40 mm for each case) denotes the wavenumber of the two interfaces, and L_0, the initial layer thickness, is defined as the distance between the average positions of I1 and I2. The detailed values of a_0^{I1}, a_0^{I2} and L_0 for each perturbed case are listed in table 1. Both in-phase (IP) and anti-phase (AP) perturbed cases involve four scenarios, with $L_0 = 50$, 30, 10 and 5 mm, designed to examine the effect of thickness variation on finger collisions. We define the in-phase (anti-phase) cases with $L_0 = 50$, 30, 10 and 5 mm as cases L50-IP (L50-AP), L30-IP (L30-AP), L10-IP (L10-AP) and L5-IP (L5-AP), respectively. As depicted in figure 1, both I1 and I2 consist of three-wavelength sinusoidal perturbations connecting two flat sections of 10 mm on each side. These flat sections are introduced to minimize the wall effects of the shock tube (Brouillette & Sturtevant 1994; Reilly *et al.* 2015) and have negligible influence on the evolution of the middle sinusoidal perturbation (Luo *et al.* 2019). The reflection distance L_{re}, defined as the distance from the average position of I2 to the reflecting wall, is consistently set at 100 mm for all cases. This distance ensures that at the time of reshock arrival, the amplitude growth for both interfaces remains in the initial stage so that the existing theories are expected to describe the perturbation growth during finger collisions. Additionally, four unperturbed cases, with $L_0 = 50$, 30, 10 and 5 mm, denoted as cases L50-1D, L30-1D, L10-1D and L5-1D, are designed to analyse the wave dynamics and interface motions during the finger collision process. In this work, the values of L_0/λ for $L_0 = 50$, 30, 10 and 5 mm are 1.25, 0.75, 0.25 and 0.125, respectively. For incompressible fluids, Taylor (1950) indicated that when $L_0/\lambda < 1/3$, the coupling
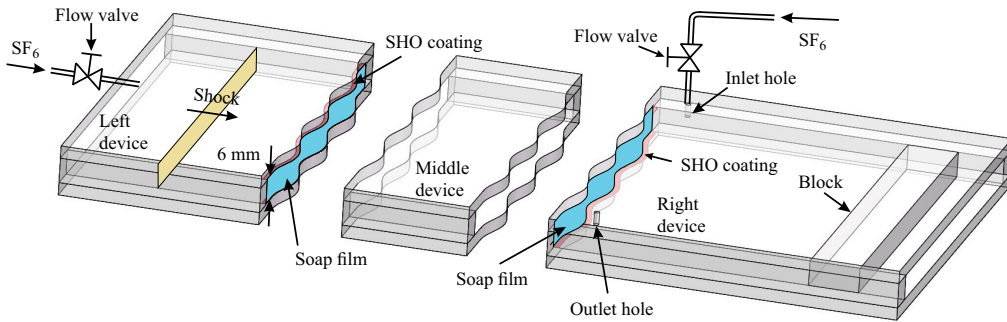
Figure 2. Schematic of the interface formation device. Here, 'SHO coating' indicates the super-hydrophobic-oleophobic coating, used to constrain the soap film to the designed shape.

between the two interfaces becomes significant. Based on this, we classify the cases with $L_0 = 50$ and 30 mm as the larger L_0 cases, and those with $L_0 = 10$ and 5 mm as the smaller L_0 cases.

Figure 2 depicts the interface formation device used to generate the perturbed soap-film interfaces. This device comprises three components: left, middle, and right devices, all fabricated by transparent acrylic plates. The precision of the engraving machine used for processing the interface formation device is 0.02 mm, significantly smaller than the interface amplitude of 2 mm and the wavelength of 40 mm. Therefore, the differences in phase and amplitude due to processing among different cases can be considered negligible. For the perturbed case, the edges of the acrylic plates are pre-carved into the sinusoidal shape. To constrain the soap film to the designed shape, a super-hydrophobic-oleophobic (SHO) material is applied to the sinusoidal edges of the left and right devices (Li *et al.* 2023; Gao *et al.* 2024). The SHO coating does not introduce obstacles in the flow field (Wang *et al.* 2022) and thereby has no effect on the interface evolution. Then a rectangular brush, dipped in a suitable amount of soap solution along its borders, is pulled along the sinusoidal edges. Finally, soap-film interfaces are generated on the left and right devices, as presented in figure 2. Note that high-wavenumber perturbations would occur at the developing interface due to the breakup of the soap film caused by the shock impact. The scale of these perturbations is comparable to the size of the shock-induced atomized soap droplets. Previous studies have shown that at Mach number approximately 1.26, the size of the atomized droplets is approximately 35 μm (Ranjan *et al.* 2009), much smaller than the interface wavelength 40 mm. Thus the influence of the high-wavenumber perturbations induced by the atomized droplets is negligible.

Gas SF_6 is inflated into the left and right devices to generate an SF_6/air/SF_6 fluid layer. When the soap-film interfaces are prepared, SF_6 is first charged into the right device through the inlet hole, and the air is discharged from the outlet hole, as illustrated in figure 2. Subsequently, the left, middle and right devices are connected through a drawer device, then the combined unit is inserted into the test section of the shock tube. Gas SF_6 is injected into the left device using a tube inserted into the shock tube, ultimately generating an SF_6/air/SF_6 fluid layer. During the SF_6 inflation process, a flow valve is used to maintain a suitable inflation rate, thus preserving the integrity of the soap film and ensuring the repeatability of experiments. For all experimental runs, the volume fraction of SF_6 on the left (right) side of I1 (I2) is maintained at 67.5 % $\pm$ 1.0 % (87.2 % $\pm$ 1.0 %). The soap film allows a small amount of SF_6 to diffuse into the middle device, resulting in a volume fraction of SF_6 within the layer of 3 % $\pm$ 0.5 %. According to the densities

of gases inside and outside the fluid layer, the Atwood numbers ($= (\rho_h - \rho_l)/(\rho_h + \rho_l)$, with ρ_h and ρ_l the densities of the heavy and light fluids) for I1 and I2 are determined as 0.54 ± 0.01 and 0.60 ± 0.01, respectively.

The experiments are conducted in the horizontal shock tube designed by our group, which has proven its feasibility and reliability in reshock experiments (Cong *et al.* 2022; Guo *et al.* 2022*a*). The driver and driven sections of the shock tube are initially separated by a thin polyethylene terephthalate (PET) film. Air is then pumped into the driver section using an air compressor. Upon reaching the endurance limit of the PET film, it breaks, resulting in the formation of an incident shock that propagates along the driven section. When the incident shock arrives at the test section, it first traverses the fluid layer and then encounters a rigid wall that is formed by an acrylic block located 100 mm downstream of I2 (see figure 2). Subsequently, a reflected shock (namely, reshock) is generated. The reshock returns to impact the developing fluid layer, resulting in complex wave–interface interactions and additional vorticity deposition. In this work, the incident shock and the reshock have Mach numbers 1.262 and 1.268, respectively. The flow field is recorded by a schlieren system combined with a high-speed camera (FASTCAM SA-Z, Photron Limited). Further details about the schlieren system can be found in the previous work (Guo *et al.* 2022*a*). The frame rate of the camera is 60 000 frames per second, and the exposure time is 0.6 µs. The pixel resolution is 0.29 mm per pixel. The ambient temperature and pressure are 291.1 ± 1 K and 101.0 kPa, respectively.

3. The 1-D wave dynamics and interface motions

In this section, the wave dynamics and interface motions in unperturbed cases are investigated both experimentally and theoretically. Since the wave–wave and wave–interface interactions are sensitive to L_0, we will demonstrate separately the results for the larger (L50-1D, L30-1D) and smaller (L10-1D, L5-1D) L_0 cases.

3.1. *Larger layer thickness cases*

Case L50-1D is taken as an example to illustrate the motions of waves and interfaces for the larger L_0 cases. Figure 3 shows the schlieren images and the corresponding sketches for case L50-1D at different moments. The x–t diagram for this case, a plot of the spatial location of various waves along with the interfaces on the x-axis as a function of time on the y-axis, is presented in figure 4. Note that for clarity, only the waves inside and on the right side of the fluid layer are included, since these waves interact directly with the interfaces. As shown in figure 4(*a*), the interactions of the incident shock (IS) and the fluid layer lead to generations of multiple transmitted shocks (TS$_a$, TS$_1$, TS$_2$) and reflected shocks (RS$_a$, RS$_b$). Then TS$_1$ and TS$_2$ successively reach the end wall, generating the reflected shocks RTS$'_1$ and RTS$'_2$ (see figure 3*b*). Shock RTS$'_2$ catches up with RTS$'_1$ before they arrive at I2, then the two shocks merge into one shock, denoted as the first reshock RS$_1$ (see figure 3*c*). The interactions of RS$_1$ and the fluid layer result in multiple waves, including the reverberating shocks (TS$_b$, RS$_c$, RS$_d$), the reflected rarefaction wave (RW$_1$) and the transmitted shock (TS$_3$). Wave RW$_1$ and shock TS$_3$ propagate towards the end wall, subsequently leading to complex shock–rarefaction–wall interactions, and the details of these wave dynamics are magnified in figure 4(*b*). After the shock–rarefaction–wall interactions, the reflected rarefaction wave, denoted as RRW$_1$, and the second reshock, denoted as RS$_2$, are generated. Wave RRW$_1$ and shock RS$_2$ successively collide with I2, resulting in the formations of transmitted waves including a rarefaction wave (TRW$_a$) and
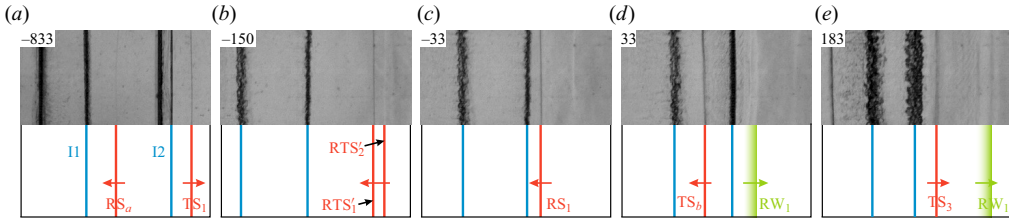
Figure 3. Schlieren images (top) and corresponding sketches (bottom) for case L50-1D. Numbers denote time in μs.
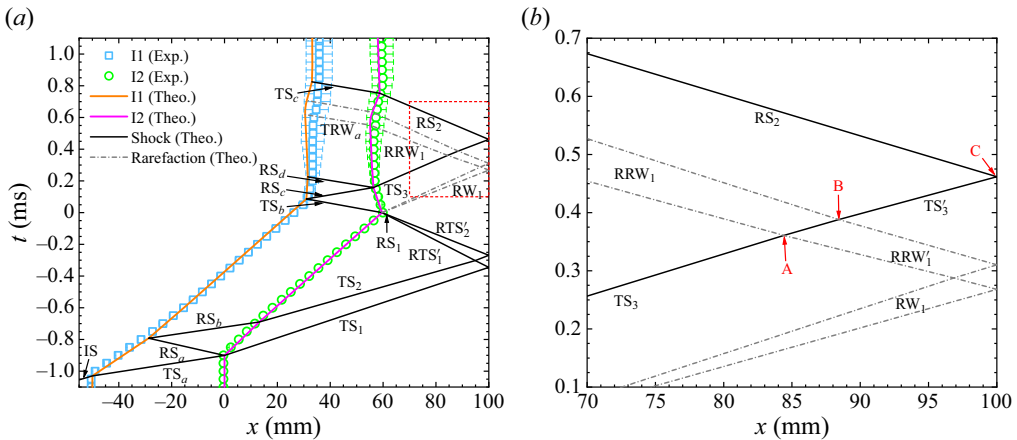
Figure 4. (*a*) The *x–t* diagram for case L50-1D. (*b*) Enlarged view of the shock–rarefaction–wall interactions marked with red dashed lines. Here, IS is the incident shock; RS_1 and RS_2 are the first and second reshocks; $TS_{a,b,c}$ and $TS_{1,2,3}$ are the transmitted shocks; $RS_{a,b,c,d}$ and $RTS'_{1,2}$ are the reflected shocks; RW_1, RRW'_1, RRW_1 and TRW_a are the rarefaction waves.

a shock (TS_c). Overall, after multiple interactions of reshocks and rarefaction waves with the fluid layer, both interfaces approach near-stationary states in the late stage.

Note that in figure 4(*a*), we focus only on the reverberating waves that are significant for the interface motions, although theoretically, an infinite number of reverberating waves exist within the fluid layer. Based on the experimental conditions of this work, Mach numbers for RS_b, RS_d and TS_c are determined as 1.012, 1.013 and 1.038, respectively, through 1-D gas dynamics theories (Han & Yin 1993). Subsequent reverberating shocks following these three shocks possess Mach numbers below 1.01, resulting in the induced jump velocity not exceeding 4 m s^{-1}. This velocity is much smaller than the velocity (>60 m s^{-1}) induced by the incident shock or reshock, indicating limited effects on the interface motions. Consequently, reverberating shocks after RS_b, RS_d and TS_c are not included in figure 4. The rarefaction waves RRW_1 and TRW_a induce interface velocity variations 27.0 m s^{-1} and 19.4 m s^{-1}, respectively. The subsequent reverberating rarefaction waves induce interface velocity variations less than 5 m s^{-1}, indicating limited influence on the interface movements. Therefore, the rarefaction waves after TRW_a are not considered in figure 4.

The 1-D flow for a reshocked light fluid layer, as presented in figure 4, involves the shock–interface interaction, rarefaction–interface interaction, shock–shock interaction, rarefaction–rarefaction interaction, shock–rarefaction interaction, shock–wall interaction
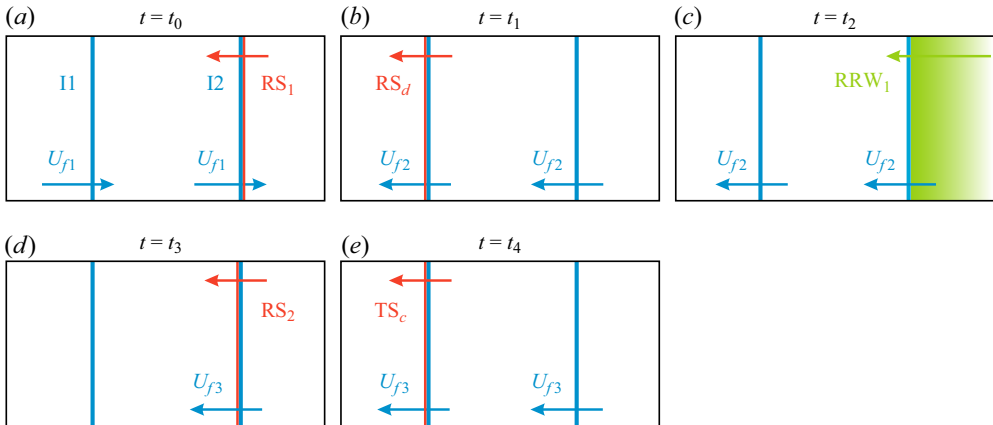
Figure 5. Sketches of wave–interface interactions at t_0–t_4: (*a*) the moment when RS$_1$ arrives at I2; (*b*) the moment when RS$_d$ arrives at I1; (*c*) the moment when the head of RRW$_1$ arrives at I2; (*d*) the moment when RS$_2$ arrives at I2; (*e*) the moment when TS$_c$ arrives at I1. Here, U_{f1} (U_{f2} and U_{f3}) denotes the asymptotic velocity for both interfaces after multiple interactions of IS (RS$_1$ and RS$_2$) and its subsequent reverberating waves with the layer.

and rarefaction–wall interaction. The fundamental relations for the wave–wave and wave–interface interactions have been outlined in previous publications on gas dynamics (Han & Yin 1993; Zucker & Biblarz 2019). Based on these fundamental relations, Liang & Luo (2022*b*) developed models to describe the motions of shocks and interfaces in a singly shocked light layer case. However, the flow of a reshocked light layer case is much more complex than that (involving only the shock–interface interaction) in the single shock condition. To characterize the motions of waves and interfaces for the reshocked light fluid layer, several specific times, including t_0, t_1, t_2, t_3 and t_4, are defined, as illustrated in figure 5. Specifically, t_0, defined as time zero ($t_0 = 0$), denotes the moment when RS$_1$ arrives at I2, t_1 denotes the moment when RS$_d$ arrives at I1, t_2 denotes the moment when the head of RRW$_1$ arrives at I2, t_3 denotes the moment when RS$_2$ arrives at I2, and t_4 denotes the moment when TS$_c$ arrives at I1. The t_1, t_2, t_3 and t_4 times can be expressed, respectively, as follows:

$$t_1 = t_{RSd}^{I1} = \frac{x_{RSc}^{I2} - x_{TSb}^{I1} - V_{RSd}t_{RSc}^{I2} + (U_{f1} + \Delta U_{TSb}^{I1})t_{TSb}^{I1}}{U_{f1} + \Delta U_{TSb}^{I1} - V_{RSd}}, \quad (3.1a)$$

$$t_2 = t_{hRRW1}^{I2} = \frac{x_A - x_{RSc}^{I2} + U_{f2}t_{RSc}^{I2} - V_{hRRW1}t_A}{U_{f2} - V_{hRRW1}}, \quad (3.1b)$$

$$t_3 = t_{RS2}^{I2} = \frac{x_C - x_{tRRW1}^{I2} + (U_{f2} + \Delta U_{RRW1}^{I2})t_{tRRW1}^{I2} - V_{RS2}t_C}{U_{f2} + \Delta U_{RRW1}^{I2} - V_{RS2}}, \quad (3.1c)$$

$$t_4 = t_{TSc}^{I1} = \frac{x_{RS2}^{I2} - x_{tTRWa}^{I1} + (U_{f2} + \Delta U_{TRWa}^{I1})t_{tTRWa}^{I1} - V_{TSc}t_{RS2}^{I2}}{U_{f2} + \Delta U_{TRWa}^{I1} - V_{TSc}}. \quad (3.1d)$$

In this work, we use t, x, U, ΔU, V and g to denote time, location, interface velocity, interface velocity variation, wave velocity and interface acceleration, respectively. The meanings of various physical quantities involved in (3.1*a*)–(3.1*d*) are outlined in table 2. The specific values of t_0–t_4 calculated by (3.1*a*)–(3.1*d*) are provided in table 3.

1000 A87-8

Symbols	Meanings
t_1 (t_{RSd}^{I1})	The time when RS_d arrives at I1.
t_2 (t_{RS2}^{I2})	The time when RS_2 arrives at I2.
t_3 (t_{TSc}^{I1})	The time when TS_c arrives at I1.
t_4 (t_{RSc}^{I2})	The time when RS_c arrives at I2.
t_{hRRW1}^{I2}	The time when the head of RRW_1 arrives at I2.
t_{tRRW1}^{I2}	The time when the tail of RRW_1 arrives at I2.
t_{hTRWa}^{I1}	The time when the head of TRW_a arrives at I1.
t_{tTRWa}^{I1}	The time when the tail of TRW_a arrives at I1.
t_A	The time corresponding to point A in figures 4(*b*) and 6(*b*).
t_B	The time corresponding to point B in figures 4(*b*) and 6(*b*).
t_C	The time corresponding to point C in figures 4(*b*) and 6(*b*).
t_D	The time corresponding to point D in figure 6(*b*).
x_{RSc}^{I2}	The location of I2 at t_{RSc}^{I2}.
x_{TSb}^{I1}	The location of I1 at t_{TSb}^{I1}.
x_{RS2}^{I2}	The location of I2 at t_{RS2}^{I2}.
x_{hRRW1}^{I2}	The location of I2 at t_{hRRW1}^{I2}.
x_{tRRW1}^{I2}	The location of I2 at t_{tRRW1}^{I2}.
x_{hTRWa}^{I1}	The location of I1 at t_{hTRWa}^{I1}.
x_{tTRWa}^{I1}	The location of I1 at t_{tTRWa}^{I1}.
x_A	The *x*-coordinate corresponding to point A in figures 4(*b*) and 6(*b*).
x_B	The *x*-coordinate corresponding to point B in figures 4(*b*) and 6(*b*).
x_C	The *x*-coordinate corresponding to point C in figures 4(*b*) and 6(*b*).
x_D	The *x*-coordinate corresponding to point D in figure 6(*b*).
U_{f1}	The asymptotic velocity for both interfaces after RS_b leaves I2.
U_{f2}	The asymptotic velocity for both interfaces after RS_d leaves I1.
U_{f3}	The asymptotic velocity for both interfaces after TS_c leaves I1.
ΔU_{TSb}^{I1}	The jump velocity of I1 induced by TS_b.
ΔU_{RRW1}^{I2}	The velocity variation of I2 induced by RRW_1.
ΔU_{TRWa}^{I1}	The velocity variation of I1 induced by TRW_a.
V_{RSd}	The velocity of RS_d.
V_{RS2}	The velocity of RS_2.
V_{TSc}	The velocity of TS_c.
V_{hRRW1}	The velocity of the head of RRW_1.
V_{tRRW1}	The velocity of the tail of RRW_1.
V_{tTRWa}	The velocity of the tail of TRW_a.
g_{RRW1}^{I2}	The average acceleration of I2 imposed by RRW_1.
g_{TRWa}^{I1}	The average acceleration of I1 imposed by TRW_a.

Table 2. Glossary for various physical quantities involved in this work.

The acceleration of a shock on an interface is instantaneous, while a rarefaction wave has a width, thus its interaction with an interface is a continuous process. Since the duration of the rarefaction wave accelerating the interface is relatively short in this work (no more than 100 µs), here, the average acceleration is employed to characterize the rarefaction–interface interaction (Morgan, Likhachev & Jacobs 2016; Morgan *et al.* 2018; Liang & Luo 2021; Cong *et al.* 2022). The time (Δt_{RRW1}^{I2}) of passage for RRW_1 through

Case	L50-1D	L30-1D	L10-1D	L5-1D
t_0 (µs)	0	0	0	0
t_1 (µs)	359	215	7	3
t_2 (µs)	552	540	543	531
t_3 (µs)	753	684	625	599
t_4 (µs)	927	784	651	613
Δt_{RRW1}^{I2} (µs)	82	94	81	69
Δt_{TRWa}^{I1} (µs)	89	84	82	64
g_{RRW1}^{I2} (m s^{-2})	3.29×10^5	2.87×10^5	3.31×10^5	3.23×10^5
g_{TRWa}^{I1} (m s^{-2})	2.18×10^5	2.31×10^5	2.32×10^5	2.67×10^5

Table 3. Values of the specific physical quantities for different cases determined by the 1-D theory ((3.1a)–(3.6c)). Here, t_0 denotes the time when RS$_1$ arrives at I2; t_1 denotes the time when RS$_d$ arrives at I1; t_2 denotes the time when the head of RRW$_1$ arrives at I2; t_3 denotes the time when RS$_2$ arrives at I2; t_4 denotes the time when TS$_c$ arrives at I1; Δt_{RRW1}^{I2} (Δt_{TRWa}^{I1}) denotes the time of passage for RRW$_1$ (TRW$_a$) through I2 (I1); and g_{RRW1}^{I2} (g_{TRWa}^{I1}) denotes the average acceleration imposed on I2 (I1) by RRW$_1$ (TRW$_a$).

I2, and the average acceleration (g_{RRW1}^{I2}) imposed on I2, can be expressed, respectively, as

$$\Delta t_{RRW1}^{I2} = \frac{x_B - x_{hRRW1}^{I2} + (t_{hRRW1}^{I2} - t_B)V_{tRRW1}}{U_{f2} + \frac{1}{2}\Delta U_{RRW1}^{I2} - V_{tRRW1}}, \tag{3.2a}$$

$$g_{RRW1}^{I2} = \frac{\Delta U_{RRW1}^{I2}}{\Delta t_{RRW1}^{I2}}. \tag{3.2b}$$

The time (Δt_{TRWa}^{I1}) of passage for TRW$_a$ through I1, and the average acceleration (g_{TRWa}^{I1}) imposed on I1, can be expressed, respectively, as

$$\Delta t_{TRWa}^{I1} = \frac{x_{tRRW1}^{I2} - x_{hTRWa}^{I1} + (t_{hTRWa}^{I1} - t_{tRRW1}^{I2})V_{tTRWa}}{U_{f2} + \frac{1}{2}\Delta U_{TRWa}^{I1} - V_{tTRWa}}, \tag{3.3a}$$

$$g_{TRWa}^{I1} = \frac{\Delta U_{TRWa}^{I1}}{\Delta t_{TRWa}^{I1}}. \tag{3.3b}$$

The detailed values of Δt_{RRW1}^{I2}, g_{RRW1}^{I2}, Δt_{TRWa}^{I1} and g_{TRWa}^{I1} determined by (3.2a)–(3.3b) are listed in table 3.

In short, the motions of waves and interfaces for the reshocked light fluid layer in five stages can be described by a 1-D theory. As depicted in figure 5, stage 1 occurs during the time interval $t_0 < t < t_1$, during which both interfaces experience multiple reshock–interface interactions, leading to a decrease in their velocity from U_{f1} ($\sim$68 m s^{-1}) to U_{f2} ($\sim$3 m s^{-1}). Stage 2 occurs during the time interval $t_1 < t < t_2$, during which both interfaces move at a constant velocity U_{f2}. Stage 3 occurs during the time interval $t_2 < t < t_3$, during which the rarefaction–interface interactions dominate. Stage 4 occurs during the time interval $t_3 < t < t_4$, during which the velocities of both interfaces decrease to U_{f3} ($\sim$0 m s^{-1}) due to the reshock–layer interaction. Stage 5 occurs when $t_4 < t$, during which both interfaces move at a constant velocity U_{f3}. Figure 4(a) presents

the comparison of interface motions for case L50-1D between the experimental results and 1-D theoretical predictions in different stages. Good agreement between experimental and theoretical results is achieved.

3.2. *Smaller layer thickness cases*

Case L10-1D is taken as an example to illustrate the motions of waves and interfaces for the smaller L_0 cases. The x–t diagram for case L10-1D is presented in figure 6(a), with the shock–rarefaction–wall interactions enclosed by the red dashed lines magnified in figure 6(b). In comparison with the x–t diagram shown in figure 4, there are two differences in wave behaviours in figure 6. First, TS_1 and TS_2 merge into TS_{12} before reaching the end wall. Second, before RS_2 and RRW_1 reach I2, RS_2 catches up with RRW_1, transforming the rarefaction wave region overtaken by the shock into the post-shock region (Han & Yin 1993; Gao *et al.* 2024). As a result, RS_2 becomes the tail of RRW_1, and thereby TS_c becomes the tail of TRW_a. For both larger and smaller L_0 cases, the Mach number of RS_1 is approximately 1.268, indicating that the difference in merging time for TS_1 and TS_2 has almost no influence on the intensity of RS_1. However, RS_2 catching up with RRW_1 and TS_c catching up with TRW_a result in differences in the calculations of t_3 and t_4 between the larger and smaller L_0 cases. The t_3 and t_4 values in cases L10-1D and L5-1D can be expressed, respectively, as follows:

$$t_3 = t_{RS2}^{I2} = \frac{-\omega_1 + (\omega_1^2 - 4\delta_1\sigma_1)^{0.5}}{2\delta_1}, \tag{3.4a}$$

$$t_4 = t_{TSc}^{I1} = \frac{-\omega_2 + (\omega_2^2 - 4\delta_2\sigma_2)^{0.5}}{2\delta_2}, \tag{3.4b}$$

with

$$\delta_1 = \tfrac{1}{2}g_{RRW1}^{I2}, \tag{3.5a}$$

$$\omega_1 = -g_{RRW1}^{I2}t_{hRRW1}^{I2} + U_{f2} - V_{RS2}, \tag{3.5b}$$

$$\sigma_1 = \tfrac{1}{2}g_{RRW1}^{I2}(t_{hRRW1}^{I2})^2 + U_{f2}t_{hRRW1}^{I2} + V_{RS2}t_D + x_{hRRW1}^{I2} - x_D, \tag{3.5c}$$

and

$$\delta_2 = \tfrac{1}{2}g_{TRWa}^{I1}, \tag{3.6a}$$

$$\omega_2 = -g_{TRWa}^{I1}t_{hTRWa}^{I1} + U_{f2} - V_{TSc}, \tag{3.6b}$$

$$\sigma_2 = \tfrac{1}{2}g_{TRWa}^{I1}(t_{hTRWa}^{I1})^2 + U_{f2}t_{hTRWa}^{I1} + V_{TSc}t_3 + x_{hTRWa}^{I1} - x_{RS2}^{I2}. \tag{3.6c}$$

The meanings of quantities in (3.4a)–(3.6c) are described in table 2. Notably, for cases L10-1D and L5-1D, (3.1a)–(3.1b) are still effective in describing t_1 and t_2, and (3.2a)–(3.3b) are applicable for describing the rarefaction–interface interactions. The detailed values of t_0–t_4, Δt_{RRW1}^{I2}, Δt_{TRWa}^{I1}, g_{RRW1}^{I2} and g_{TRWa}^{I1} in cases L10-1D and L5-1D are listed in table 3.

In short, the 1-D theory quantifies the specific times t_3 and t_4 in cases L10-1D and L5-1D, which have different calculations from those in cases L50-1D and L30-1D. Based on the specific times t_0, t_1, t_2, t_3 and t_4, the interface motions after reshock for cases L10-1D and L5-1D can also be classified into five stages, as described in § 3.1. Figure 6(a) presents the comparison of interface motions for case L10-1D between the experiments
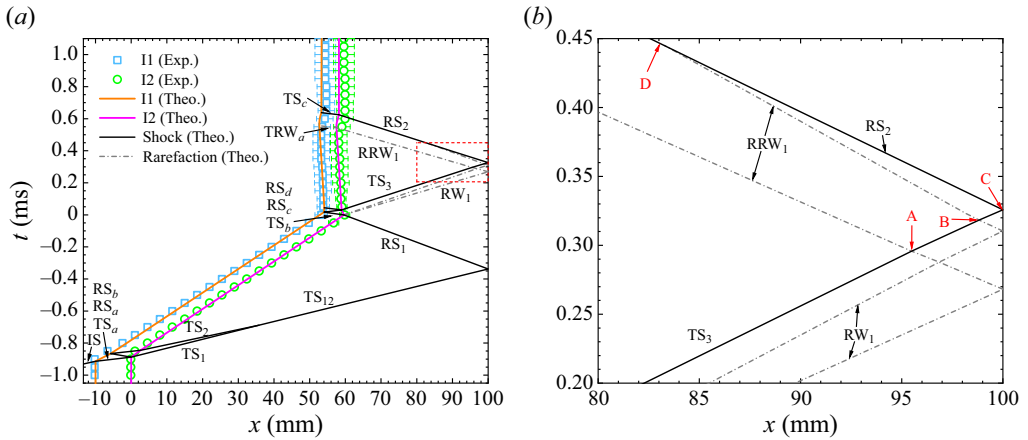
Figure 6. (*a*) The *x–t* diagram for case L10-1D. (*b*) Enlarged view of the shock–rarefaction–wall interactions marked with red dashed lines.

and the 1-D theory in different stages. It is observed that there is good agreement between experimental and theoretical results.

4. Experimental analyses of finger collisions

4.1. *Morphology of interface evolution*

Figure 7 shows the evolution of the in-phase perturbed cases with varying initial layer thicknesses. Notably, a resemblance in interface morphology is observed between cases L50-IP and L30-IP, as well as between cases L10-IP and L5-IP. Here, we take case L30-IP as an example to illustrate the interface evolution for both cases L50-IP and L30-IP. As depicted in figure 7(*b*), I1 initially experiences phase reversal due to its heavy/light configuration relative to the incident shock. Before the first reshock (RS_1) arrival, I1 and I2 transition from an initially in-phase state to an anti-phase state ($-17\ \mu s$). Subsequently, RS_1 and its transmitted shock sequentially strike I2 and I1, reversing I2's phase while promoting I1's development. The I1 spike moves downstream and eventually catches up with the I2 bubble, resulting in a spike–bubble rear-end collision (SBC) ($553\ \mu s$). The I2 spike gradually develops upstream, leading to another SBC ($1250\ \mu s$). At late times, the SBCs yield periodically arranged finger structures, fostering a nearly symmetrical expansion of the mixing zone (1250–$2350\ \mu s$).

As illustrated in figures 7(*c*) and 7(*d*), the interface evolution for cases L10-IP and L5-IP exhibits distinctions compared with cases L50-IP and L30-IP. Specifically, in cases L10-IP and L5-IP, the SBC occurs earlier, resulting in a more complete merging of the two interfaces. Notably, upstream of the mixing zone, the I1 bubble and the I2 spike gradually merge into a spike-like structure, while downstream, the I1 spike and the I2 bubble gradually merge into a bubble-like structure (841–$1241\ \mu s$). The asymmetric development of these spike- and bubble-like structures leads to the evolution of the mixing zone closely resembling that of a shocked single interface (2341 and $2345\ \mu s$) (Jacobs & Krivets 2005; Morgan *et al.* 2012; Liu *et al.* 2018).

Figure 8 shows the evolution of the anti-phase perturbed cases with varying initial layer thicknesses. In case L50-AP, as illustrated in figure 8(*a*), I1 inverts its phase after the incident shock impact. Subsequently, the two interfaces transition into an in-phase state
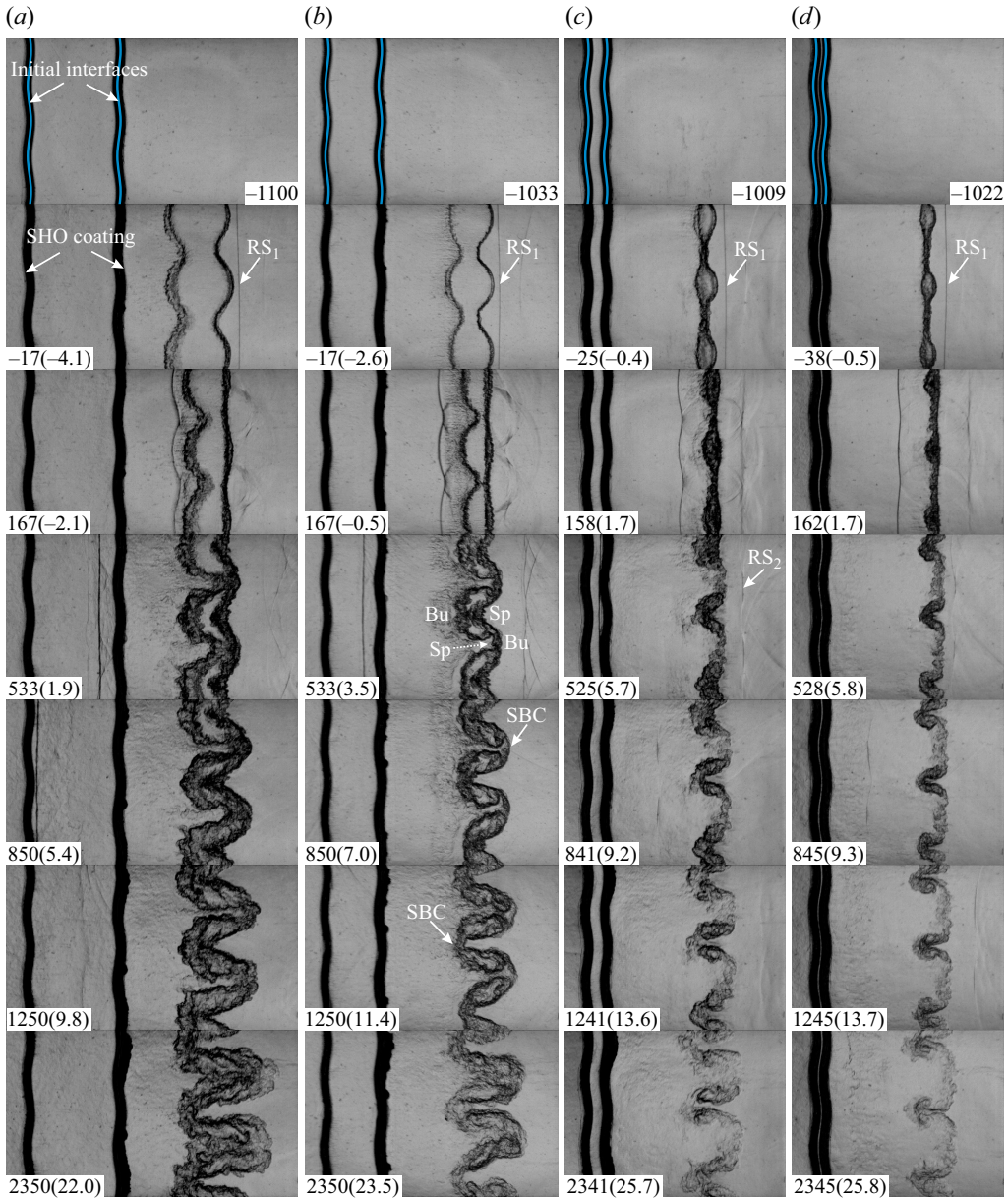
Figure 7. Schlieren images of interface evolution for cases (*a*) L50-IP, (*b*) L30-IP, (*c*) L10-IP and (*d*) L5-IP. Here, RS_1 and RS_2 are the first and second reshocks; 'Sp' and 'Bu' indicate spikes and bubbles; and SBC denotes the spike–bubble rear-end collision. Numbers outside and inside parentheses represent dimensional and dimensionless time, respectively, and similarly hereinafter. The unit of dimensional time is µs, and dimensionless time is expressed as $k\,\Delta U_f(t - t_1)$, which is introduced in §4.2.

before the RS_1 arrival (-42 µs). After the impact of RS_1, I2 undergoes a phase reversal so that its spike continuously moves upstream. Eventually, the spikes of I1 and I2 encounter each other, leading to a spike–spike head-on collision (SSC) (530 µs). In this scenario, the impact force of spikes for both interfaces is comparable, resulting in a significant inhibition of the spike developments. In contrast, the bubbles of both interfaces continuously develop
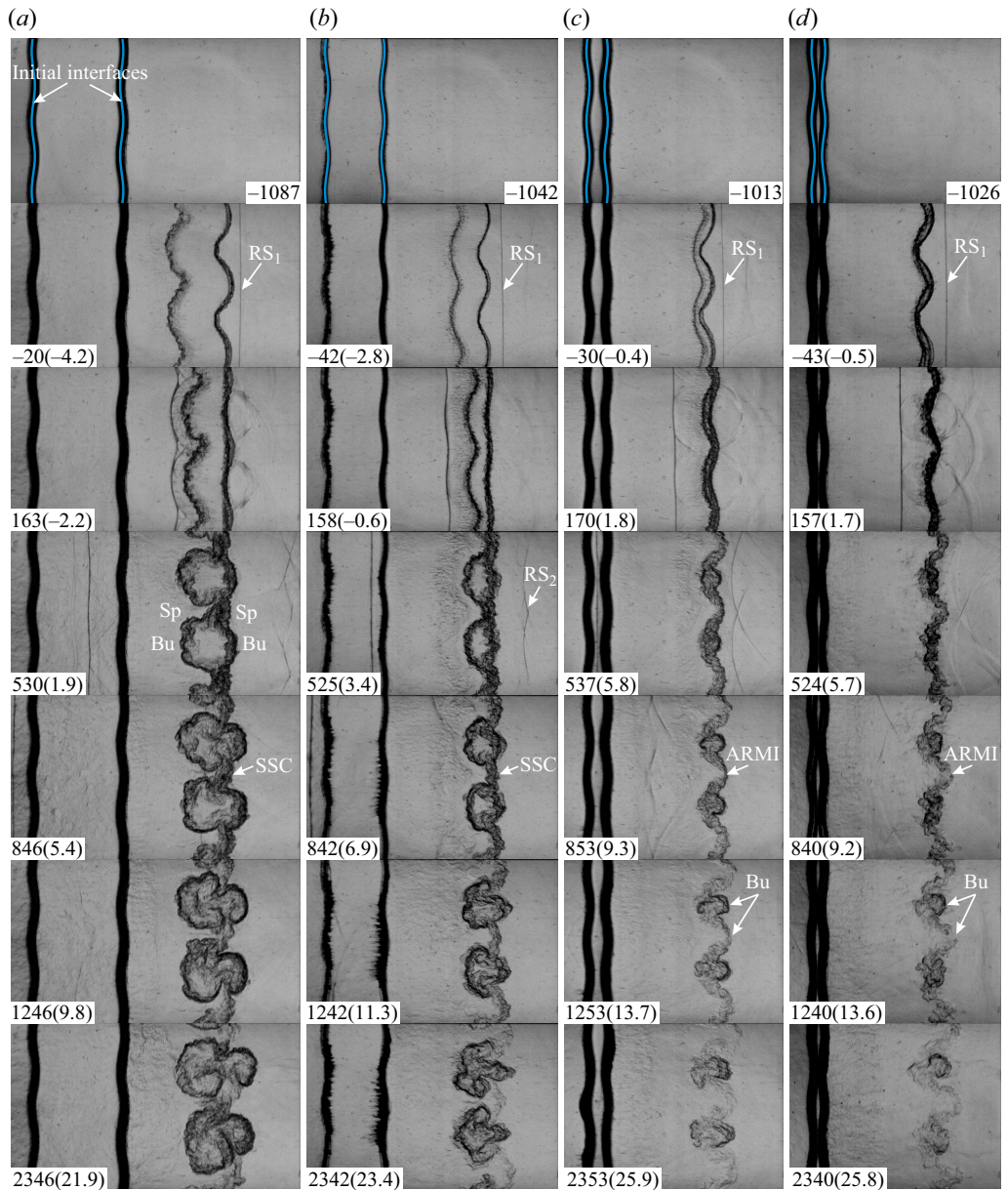
Figure 8. Schlieren images of interface evolution for cases (*a*) L50-AP, (*b*) L30-AP, (*c*) L10-AP and (*d*) L5-AP. Here, RS_1 and RS_2 are the first and second reshocks; 'Sp' and 'Bu' indicate spikes and bubbles; SSC denotes the spike–spike head-on collision; and ARMI denotes the abnormal RMI such that I2 cannot reverse its phase due to SSC, resulting in formations of two bubbles at I2, as observed in panels (*c*,*d*) at $t = 1253$ and $1240\,\mu s$.

after SSC, and at late times, two large bubble structures, characterized by rounded heads, emerge both upstream and downstream of the field of view (846–2346 μs).

In case L30-AP, as depicted in figure 8(*b*), the SSC occurs just as I2 undergoes a phase inversion (525 μs). In other words, the spike at I1 predominates over that at I2 during the SSC. The vortex pairs at the I1 spikes gradually develop, entraining the surrounding fluids into the vortical structure (842–2342 μs). Consequently, these vortex pairs continuously

Case	L50-IP	L30-IP	L10-IP	L5-IP	L50-AP	L30-AP	L10-AP	L5-AP
After reshock	SBC	SBC	SBC	SBC	SSC	SSC	SSC	SSC
Abnormal RMI	◯	◯	◯	◯	◯	◯	✓	✓

Table 4. Summary of types of finger collisions in different cases. The symbols ◯ and ✓ represent the absence or presence of abnormal RMI, respectively.

squeeze the adjacent bubbles at I2, resulting in the thinning of bubbles at I2 in the late stage (2342 µs).

As illustrated in figures 8(*c*) and 8(*d*), for cases L10-AP and L5-AP, the collision between I1 spikes and I2 precedes the I2 phase reversal (170 and 157 µs), thereby impeding I2 from inverting its phase. It is generally understood that a heavy/light interface would undergo phase reversal after a shock impact (Meyer & Blewett 1972; Holmes *et al.* 1999; Guo *et al.* 2022*b*). However, in cases L10-AP and L5-AP, an abnormal RMI phenomenon occurs such that I2 fails to reverse its phase due to the SSC (853 and 840 µs). As a result, in addition to the normally generated bubble structure, another bubble structure emerges at the original spike position on I2, with its tip positioned further downstream than the normal bubble tip (1253 and 1240 µs).

Table 4 summarizes the types of finger collisions after reshock for different cases. For initial in-phase cases, SBC occurs, while for initial anti-phase cases, SSC emerges. In particular, SSC results in abnormal RMI when L_0 is relatively small.

4.2. *Interface amplitude and mixing width*

Figures 9(*a*) and 9(*b*) show the dimensionless reshocked amplitude growth for both interfaces in the initial in-phase and anti-phase cases, respectively. The interface amplitude is defined as half of the distance between the bubble tip and the spike tip. For clarity, the amplitude data of I1 and I2 are presented respectively in the upper and lower halves of figures 9(*a*) and 9(*b*). Notably, the amplitude variations during the compression process resulting from the reshock–layer interaction are not included in figure 9; hence the amplitude evolution is displayed from $t = t_1$. Similar to previous reshock studies that scaled time using the interface jump velocity (Balakumar *et al.* 2012; Guo *et al.* 2022*a*), time in this work is scaled as $k \Delta U_f (t - t_1)$, where $\Delta U = |U_{f2} - U_{f1}|$ characterizes the change in layer interface velocity due to reshock–layer interactions. The amplitudes for I1 and I2 are normalized as $k |a^{I1} - a_1^{I1}|$ and $-k |a^{I2} - a_1^{I2}|$, respectively, where a_1^{I1} and a_1^{I2} represent the amplitudes for I1 and I2 at t_1, respectively.

For the initial in-phase cases, as illustrated in figure 9(*a*), the evolving amplitudes of both I1 and I2 decrease as L_0 diminishes, indicating that a smaller layer thickness is more favourable for the suppression of amplitude growth due to SBC. For the initial anti-phase cases, as presented in figure 9(*b*), the amplitude growth of I2 also shows a monotonic variation with L_0. Especially, SSC leads to nearly stagnant amplitude growth of I2 in all initial anti-phase cases from dimensionless time 5. However, unlike the initial in-phase cases, the amplitude growth of I1 does not follow a monotonic trend with L_0. This discrepancy is attributed to the abnormal RMI in cases L10-AP and L5-AP, where the suppression of spike growth is relatively weaker compared with cases L50-AP and L30-AP. As a result, the evolving amplitudes in cases L10-AP and L5-AP eventually exceed those in case L30-AP. Overall, compared with the initial in-phase cases, the
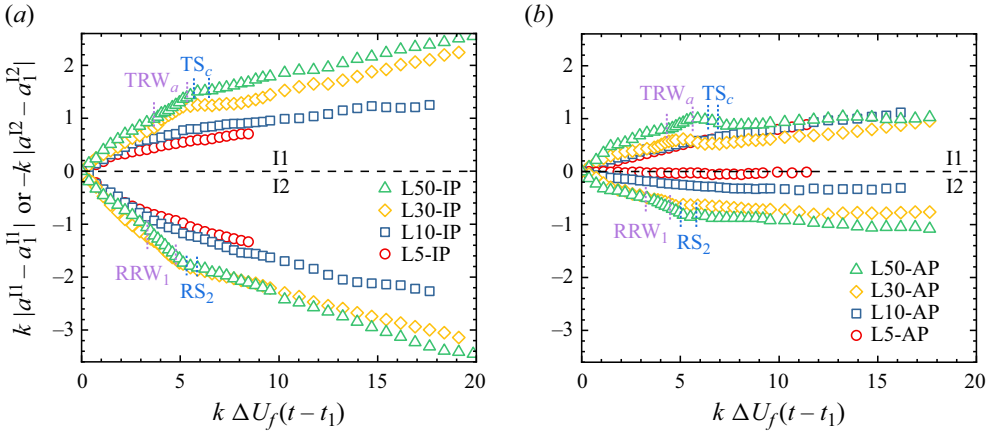
Figure 9. Dimensionless amplitude growth of I1 and I2 for the initial (*a*) in-phase and (*b*) anti-phase cases. The durations of TRW_a–I1 and RRW_1–I2 (TS_c–I1 and RS_2–I2) interactions in cases L50-IP and L50-AP are marked with purple (blue) dotted lines.

interface amplitude growth in initial anti-phase cases is more suppressed due to SSC, even resulting in stagnation of I2's amplitude growth.

Figure 10(*a*) shows the mixing widths – defined as the distance from the leftmost side of I1 to the rightmost side of I2 – as functions of time. The time axis is normalized in the same manner as the interface amplitude used in figure 9, and the mixing width is scaled as $k(h - h_1)$, with h_1 denoting the mixing width at t_1. It is observed that for the initial in-phase cases, the growth of the mixing width gradually decreases with a reduction of L_0. However, this trend is disrupted in the initial anti-phase scenarios. Specifically, due to the SSC, a substantial reduction in the mixing width growth is observed beyond dimensionless time 7 for cases L50-AP and L30-AP. Nevertheless, in cases L10-AP and L5-AP, the abnormal RMI causes the mixing width growth rates to gradually surpass those of cases L50-AP and L30-AP. After dimensionless time 13, the mixing width of case L5-AP even exceeds the values for cases L50-AP and L30-AP.

Figure 10(*b*) utilizes the reshocked linear mixing width growth rate (v_h) to normalize the time axis, a method similar to that used in the previous study on heavy fluid layers (Cong *et al.* 2022). It is observed that this scaling method collapses the mixing width data, except for cases L50-AP and L30-AP. The data for these two cases are notably lower than those for other cases, further highlighting the SSC effectiveness in suppressing the whole mixing width growth.

It is known that suppressing the development of both individual interface amplitude and overall layer mixing width is crucial for ICF (Lindl *et al.* 2014; Betti & Hurricane 2016). Figures 9 and 10 indicate that SSC effectively reduces the growth of interface amplitude and overall mixing width by suppressing spike growth, which is the primary driver of perturbation growth (Mikaelian 1998; Zhang 1998; Buttler *et al.* 2012; Dimonte *et al.* 2013). Notably, maximizing SSC effectiveness in attenuating growth requires a sufficiently large initial layer thickness. This ensures that I2 can reverse phase and develop adequately, allowing spikes to fully collide and thereby cancel out their growth.

4.3. *Effects of waves*

During finger collisions, the waves (TRW_a, RRW_1, TS_c and RS_2) continually interact with the interfaces, influencing the interface evolution. The durations of interactions of
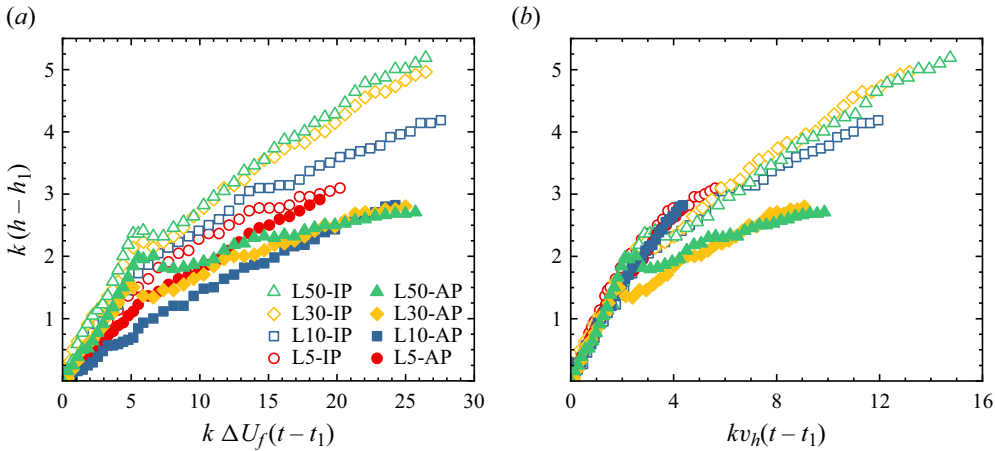
Figure 10. Dimensionless mixing width growth for different cases, scaled using (*a*) ΔU_f and (*b*) v_h on the time axis. Here, $\Delta U = |U_{f2} - U_{f1}|$ characterizes the fluid-layer interface velocity change during the reshock–layer interaction process, and v_h is the reshocked linear mixing width growth rate, obtained from linear fits of the experimental mixing width data.

different waves with both interfaces for cases L50-IP and L50-AP are marked with dotted lines, as depicted in figures 9(*a*) and 9(*b*). During the interactions of TRW_a and RRW_1 with the interfaces, the amplitude growth rates increase, while during the interactions of TS_c and RS_2 with the interfaces, the amplitude growth rates decrease. As a result, the overall amplitudes for both I1 and I2 exhibit an oscillatory growth trend. This trend is also observed in cases L30-IP and L30-AP, although the durations of wave–interface interactions are not marked for clarity. In contrast, the amplitude growth trends in cases L10-IP, L5-IP, L10-AP and L5-AP are smooth, differing from the oscillatory growth seen in the aforementioned cases. To elucidate the effects of these distinct waves (RRW_1, TRW_a, RS_2 and TS_c) on interface evolution, schematics of the interactions between the four waves and the interfaces are presented in figure 11. Figures 11(*a*–*c*) correspond to the initial in-phase cases, and figures 11(*d*–*f*) correspond to the initial anti-phase cases. Note that the two interfaces are depicted without collision to better isolate the effects of waves on each interface.

As depicted in figures 11(*a*) and 11(*d*), the influence of RRW_1 on I2 encompasses two primary aspects. (i) Wave RRW_1 strikes first the downstream side of I2 and then the upstream side, inducing interface stretching along the streamwise direction, known as the stretching effect (Cong *et al.* 2022). (ii) The RRW_1–I2 interaction induces RTI due to the imposed acceleration g_{RRW1} directed from air to SF_6 (i.e. light fluids accelerate heavy fluids). In this scenario, the vorticity resulting from the RRW_1–I2 interaction aligns with the original vorticity, thereby promoting the I2 evolution. As depicted in figures 11(*b*) and 11(*e*), TRW*a* affects I1 in two main ways: (i) the stretching effect, and (ii) the Rayleigh–Taylor stabilization (RTS) (Mikaelian 2009), resulting from the acceleration g_{TRWa} directed from SF_6 to air. It is evident that the RTS and the stretching effect exert opposing influences on the I1 amplitude growth. As shown in figure 9, in cases L50-IP and L50-AP, the I1 amplitude growth increases during the passage of TRW_a, indicating the dominance of the stretching effect between the two impacts imposed by TRW_a. As presented in figures 11(*b*) and 11(*e*), RS_2 compresses I2 and introduces vorticity opposite to that deposited by RRW_1, indicating opposing influences of RS_2 and RRW_1
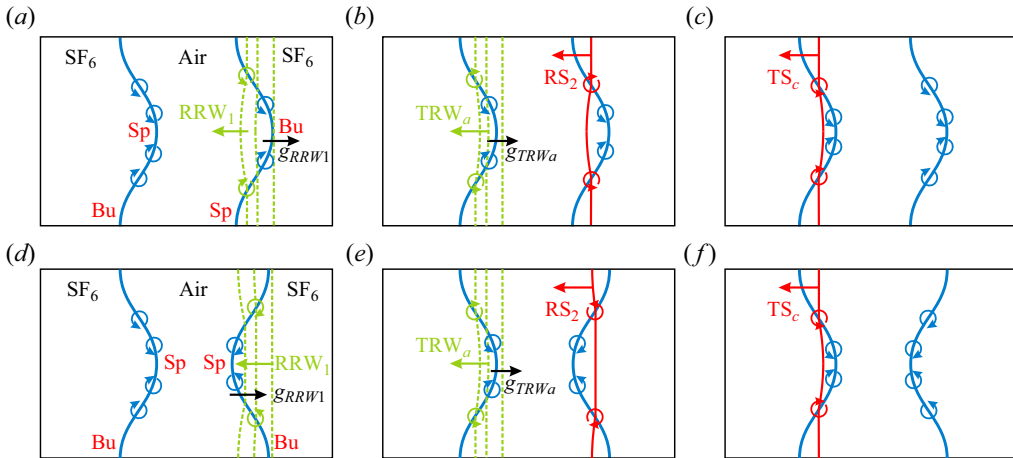
1000 A87-17

Figure 11. Schematics of the vorticity distributions resulting from the interactions between the waves (RRW_1, TRW_a, RS_2 and TS_c) and the two interfaces for initial (*a–c*) in-phase and (*d–f*) anti-phase cases.

on I2 evolution. Similarly, the effects of TS_c and TRW_a on I1 evolution oppose each other, as shown in figures 11(*b*), 11(*c*), 11(*e*) and 11(*f*). For the entire fluid layer, the stretching effect induced by rarefaction waves increases the distance between I1 and I2, thereby reducing the finger collision intensity. Conversely, the second reshock compresses the layer, enhancing the collision intensity.

The reasons for the diminished wave effects in cases L10-IP, L5-IP, L10-AP and L5-AP are explored. As discussed in the 1-D analysis in § 3.2, for the smaller L_0 cases, RS_2 (TS_c) catches up with RRW_1 (TRW_a), becoming the tail of RRW_1 (TRW_a). Subsequently, RS_2 and TS_c promptly interact with these interfaces after the interactions of RRW_1 and TRW_a. As mentioned above, the influences of RS_2 and TS_c oppose those of RRW_1 and TRW_a, effectively neutralizing these wave effects. Consequently, a relatively smooth amplitude growth trend occurs in cases L10-IP, L5-IP, L10-AP and L5-AP, as presented in figure 9.

5. Theoretical predictions

5.1. *Linear amplitude growth*

Before the collision of fingers, both interfaces exhibit linear amplitude growth, as shown in figure 9. Table 5 presents the experimental linear amplitude growth rates v_e^{I1} and v_e^{I2} for I1 and I2. These values are determined through linear fits of the experimental amplitude data, with positive or negative signs depending on the observed slopes in figure 9. Notably, both v_e^{I1} and v_e^{I2} can be regarded as the linear superposition of two components (Mikaelian 1985; Charakhch'yan 2001): (i) the amplitude growth rate before reshock, denoted as v_{bf}^{I1} and v_{bf}^{I2} for I1 and I2; and (ii) the reshock-induced amplitude growth rate, denoted as da^{I1}/dt and da^{I2}/dt for I1 and I2. Here, v_{bf}^{I1} and v_{bf}^{I2} can be obtained through linear fits of the amplitude data before reshock (see table 5 for detailed values), as performed in previous studies (Charakhch'yan 2001); da^{I1}/dt and da^{I2}/dt, directly related to the reshock–layer interaction, will be quantified theoretically.

For a shocked fluid layer separating three fluids with different densities (i.e. an A/B/C-type layer), Liang & Luo (2022*a*) extended the model of Jacobs *et al.* (1995) to the

Case	v_e^{I1}	v_e^{I2}	v_t^{I1}	v_t^{I2}	$\dfrac{\mathrm{d}a^{I1}}{\mathrm{d}t}$	$\dfrac{\mathrm{d}a^{I2}}{\mathrm{d}t}$	v_{bf}^{I1}	v_{bf}^{I2}	a_α^{I1}	a_1^{I1}	a_α^{I2}	a_β^{I2}
L50-IP	23.3 ± 1.3	-18.7 ± 1.5	24.5	-20.9	19.3	-25.7	5.1	4.8	5.6	7.2	-4.1	-1.4
L30-IP	22.0 ± 1.1	-21.6 ± 1.5	23.8	-20.6	19.5	-23.9	4.3	3.2	4.8	5.2	-3.4	-0.4
L10-IP	14.2 ± 1.2	-19.6 ± 1.4	12.8	-8.9	11.5	-11.4	1.3	2.5	1.9	1.8	-1.7	-1.15
L5-IP	11.9 ± 0.8	-17.4 ± 1.1	10.4	-10.6	9.5	-11.7	0.8	1.1	1.3	1.1	-1.8	-1.0
L50-AP	23.4 ± 1.3	-19.4 ± 1.4	24.8	-17.2	20.4	-20.0	4.3	2.8	5.6	6.4	3.4	2.0
L30-AP	14.4 ± 1.1	-14.6 ± 1.3	16.8	-15.9	12.4	-18.2	4.3	2.3	3.0	4.2	2.9	1.9
L10-AP	11.1 ± 0.9	-3.9 ± 0.8	13.9	-6.9	9.6	-10.0	4.3	3.0	2.4	2.8	2.6	2.4
L5-AP	7.4 ± 0.8	-0.5 ± 0.3	15.0	-5.2	10.7	-9.5	4.2	4.3	3.8	3.5	3.6	3.0

Table 5. Comparison of the theoretical and experimental amplitude growth rates: v_e^{I1} and v_e^{I2} are the experimental linear amplitude growth rates for I1 and I2; v_t^{I1} and v_t^{I2} are the theoretical linear amplitude growth rates for I1 and I2, obtained from (5.7a) and (5.7b); $\mathrm{d}a^{I1}/\mathrm{d}t$ and $\mathrm{d}a^{I2}/\mathrm{d}t$, the reshock-induced linear amplitude growth rates for I1 and I2, are obtained from (5.5a) and (5.5b); v_{bf}^{I1} and v_{bf}^{I2} are the experimental amplitude growth rates for I1 and I2 before reshock; a_α^{I1}, a_1^{I1}, a_α^{I2} and a_β^{I2} are the post-reshock amplitudes, as detailed in figures 12(b)–12(e). The units of velocities and lengths are m s^{-1} and mm, respectively.

following forms (the LL model) to describe the linear amplitude growth of both interfaces:

$$[\rho_1 + \rho_2 \tanh(kL_0/2)] \frac{\mathrm{d}a^{I1}}{\mathrm{d}t} + [\rho_3 + \rho_2 \tanh(kL_0/2)] \frac{\mathrm{d}a^{I2}}{\mathrm{d}t}$$
$$= k[(\rho_2 - \rho_1)a_0^{I1} \, \Delta U_i + (\rho_3 - \rho_2)a_0^{I2} \, \Delta U_t], \qquad (5.1a)$$

$$[\rho_1 + \rho_2 \coth(kL_0/2)] \frac{\mathrm{d}a^{I1}}{\mathrm{d}t} - [\rho_3 + \rho_2 \coth(kL_0/2)] \frac{\mathrm{d}a^{I2}}{\mathrm{d}t}$$
$$= k[(\rho_2 - \rho_1)a_0^{I1} \, \Delta U_i + (\rho_2 - \rho_3)a_0^{I2} \, \Delta U_t], \qquad (5.1b)$$

where $\rho_{1,3}$ and ρ_2 represent the densities of fluids outside and inside the layer, respectively. To simply the model, Liang & Luo (2022a) considered only the first two shock–interface interactions, and used the jump velocity ΔU_i (ΔU_t) to characterize the impulsive strength imparted to I1 (I2) by the incident (transmitted) shock. However, considering only the first two shock–interface interactions is likely to be insufficient, as I1 and I2 do not reach the same final velocity ($\Delta U_i \neq \Delta U_t$) (Cong *et al.* 2022; Zhang *et al.* 2022).

The LL model is modified to describe the reshock-induced linear amplitude growth rates $\mathrm{d}a^{I1}/\mathrm{d}t$ and $\mathrm{d}a^{I2}/\mathrm{d}t$. The modifications to the LL model aim to accurately characterize the reshock–layer interactions. Taking the in-phase scenario as an example, figure 12 shows the process of interactions of RS$_1$ and its subsequent reverberating shocks (TS$_b$, RS$_c$ and RS$_d$) with the two interfaces. As depicted in figure 12(a), before the RS$_1$ impact, the amplitudes of I1 and I2 are denoted as a_{bf}^{I1} and a_{bf}^{I2}, respectively, and the densities of fluids are denoted as ρ_1', ρ_2' and ρ_3', respectively. Then RS$_1$ and TS$_b$ impact I2 and I1, imposing jump velocities ΔU_{RS1}^{I2} ($= -87.9$ m s^{-1}) and ΔU_{TSb}^{I1} ($= -64.1$ m s^{-1}) on the respective interfaces, as illustrated in figures 12(b) and 12(c). After the impacts of RS$_1$ and TS$_b$, I2 and I1 reach velocities -20.4 m s^{-1} and 3.5 m s^{-1}, respectively, demonstrating a notable discrepancy between them. This indicates that considering only the first two reshock–interface interactions is insufficient for characterizing the total reshock-induced impulsive strength. As depicted in figures 12(d) and 12(e), RS$_c$ and RS$_d$ impose jump velocities ΔU_{RSc}^{I2} ($= 16.1$ m s^{-1}) and ΔU_{RSd}^{I1} ($= -5.5$ m s^{-1}) on I2 and I1, respectively.
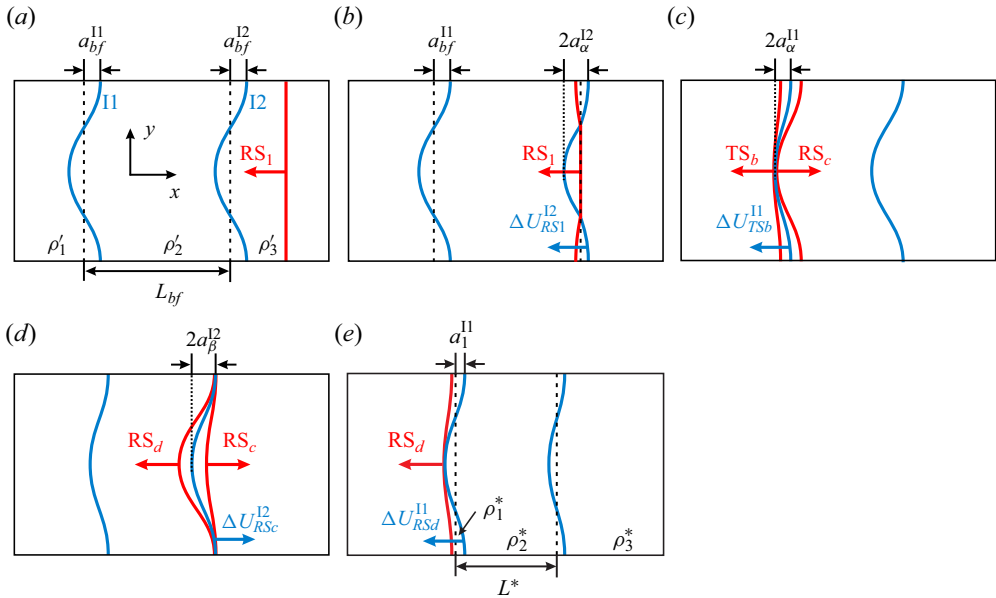
Figure 12. Schematics of the interactions between the shocks (RS_1, TS_b, RS_c and RS_d) and the two perturbed interfaces: (*a*) the moment prior to the impact of RS_1; (*b*) the moment when RS_1 arrives at the centre of I2; (*c*) the moment when TS_b completely passes through I1; (*d*) the moment when RS_c completely passes through I2; (*e*) the moment when RS_d completely passes through I1.

After the impacts of RS_c and RS_d, I2 and I1 respectively reach velocities -4.3 m s^{-1} and -2.1 m s^{-1}, with both values being very close. The jump velocities induced by the later reverberating shocks decay rapidly, not exceeding 1.5 m s^{-1}, indicating minimal influence on the interface movement. As a result, besides the first two reshock–interface interactions, two more reshock–interface interactions are considered in the modification to the LL model.

The compression effects resulting from the reshock–layer interaction are quantified through the post-reshock quantities to further modify the LL model. Notably, among the four reshock–interface interactions mentioned above, the first involves a heavy/light interface configuration, while the three remaining cases involve a light/heavy configuration. The methods proposed by Meyer & Blewett (1972) and Richtmyer (1960) have been validated for describing post-shock amplitudes in heavy/light (Holmes *et al.* 1999; Guo *et al.* 2022*a*) and light/heavy (Jacobs & Krivets 2005; Liu *et al.* 2018) configurations, respectively, and are therefore adopted in this study. Specifically, the amplitude (a_α^{I2}) for I2 after the RS_1 impact is expressed as the average of the amplitudes when RS_1 just contacts and completely passes through I2. This amplitude equals the value when RS_1 arrives at the centre of I2, as illustrated in figure 12(*b*). The post-reshock amplitudes (a_α^{I1}, a_β^{I2} and a_1^{I1}) for the three remaining cases are expressed as the amplitudes when TS_b, RS_c and RS_d completely traverse the corresponding interface, as depicted in figures 12(*c*), 12(*d*) and 12(*e*). The values for a_α^{I2}, a_α^{I1}, a_β^{I2} and a_1^{I1} obtained from experiments are listed in table 5. After the four reshock–interface interactions, the fluid densities transition from ρ_1', ρ_2' and ρ_3' to ρ_1^*, ρ_2^* and ρ_3^*, which can be determined by 1-D gas dynamics theories (Han & Yin 1993). The fluid-layer thickness (L^*) after the four

reshock–interface interactions can be expressed as

$$L^* = L_{bf} \left(1 - \frac{\Delta U_{RS1}^{I2}}{V_{TSb}} \right) \left(1 - \frac{\Delta U_{RS1}^{I2} - \Delta U_{TSb}^{I1}}{-V_{RSc} + \Delta U_{RS1}^{I2}} \right) \left(1 + \frac{\Delta U_{RS1}^{I2} + \Delta U_{RSc}^{I2} - \Delta U_{TSb}^{I1}}{V_{RSd} - \Delta U_{TSb}^{I1}} \right).$$
(5.2)

After considering the jump velocities induced by the first four reshock–interface interactions and the reshock compression effects, (5.1*a*) and (5.1*b*) are modified as

$$(R_2 + \zeta) \frac{\mathrm{d}a^{I2}}{\mathrm{d}t} + (R_1 + \zeta) \frac{\mathrm{d}a^{I1}}{\mathrm{d}t} = k(R_2 - 1)(a_\alpha^{I2} \, \Delta U_{RS1}^{I2} + a_\beta^{I2} \, \Delta U_{RSc}^{I2})$$
$$- k(R_1 - 1)(a_\alpha^{I1} \, \Delta U_{TSb}^{I1} + a_1^{I1} \, \Delta U_{RSd}^{I1}), \quad (5.3a)$$

$$(R_2 + \xi) \frac{\mathrm{d}a^{I2}}{\mathrm{d}t} - (R_1 + \xi) \frac{\mathrm{d}a^{I1}}{\mathrm{d}t} = -k(R_2 - 1)(a_\alpha^{I2} \, \Delta U_{RS1}^{I2} + a_\beta^{I2} \, \Delta U_{RSc}^{I2})$$
$$- k(R_1 - 1)(a_\alpha^{I1} \, \Delta U_{TSb}^{I1} + a_1^{I1} \, \Delta U_{RSd}^{I1}), \quad (5.3b)$$

where

$$\zeta = \tanh(kL^*/2), \quad (5.4a)$$
$$\xi = \coth(kL^*/2) = 1/\zeta, \quad (5.4b)$$
$$R_1 = \rho_1^*/\rho_2^*, \quad (5.4c)$$
$$R_2 = \rho_3^*/\rho_2^*. \quad (5.4d)$$

By solving (5.3*a*) and (5.3*b*), the reshock-induced linear amplitude growth rates $\mathrm{d}a^{I1}/\mathrm{d}t$ and $\mathrm{d}a^{I2}/\mathrm{d}t$ can be expressed as

$$\frac{\mathrm{d}a^{I1}}{\mathrm{d}t} = \frac{(2R_2\zeta + \zeta^2 + 1)E_b - (1 - \zeta^2)E_a}{2(R_2 R_1 + 1)\zeta + (\zeta^2 + 1)(R_2 + R_1)}, \quad (5.5a)$$

$$\frac{\mathrm{d}a^{I2}}{\mathrm{d}t} = \frac{-(2R_1\zeta + \zeta^2 + 1)E_a + (1 - \zeta^2)E_b}{2(R_2 R_1 + 1)\zeta + (\zeta^2 + 1)(R_2 + R_1)}, \quad (5.5b)$$

with

$$E_a = k(R_2 - 1)(a_\alpha^{I2} \, \Delta U_{RS1}^{I2} + a_\beta^{I2} \, \Delta U_{RSc}^{I2}), \quad (5.6a)$$

$$E_b = k(R_1 - 1)(a_\alpha^{I1} \, \Delta U_{TSb}^{I1} + a_1^{I1} \, \Delta U_{RSd}^{I1}). \quad (5.6b)$$

According to the linear superposition principle (Mikaelian 1985; Charakhch'yan 2001), we can obtain a linear model by summing $\mathrm{d}a^{I1}/\mathrm{d}t$ and v_{bf}^{I1}, and by summing $\mathrm{d}a^{I2}/\mathrm{d}t$ and v_{bf}^{I2}, to describe the overall amplitude growth rates for I1 and I2 after reshock:

$$v_t^{I1} = \frac{\mathrm{d}a^{I1}}{\mathrm{d}t} + v_{bf}^{I1}, \quad (5.7a)$$

$$v_t^{I2} = \frac{\mathrm{d}a^{I2}}{\mathrm{d}t} + v_{bf}^{I2}. \quad (5.7b)$$

Table 5 presents a comparison between the theoretical and experimental linear amplitude growth rates after reshock. It is observed that in most cases, the theoretical
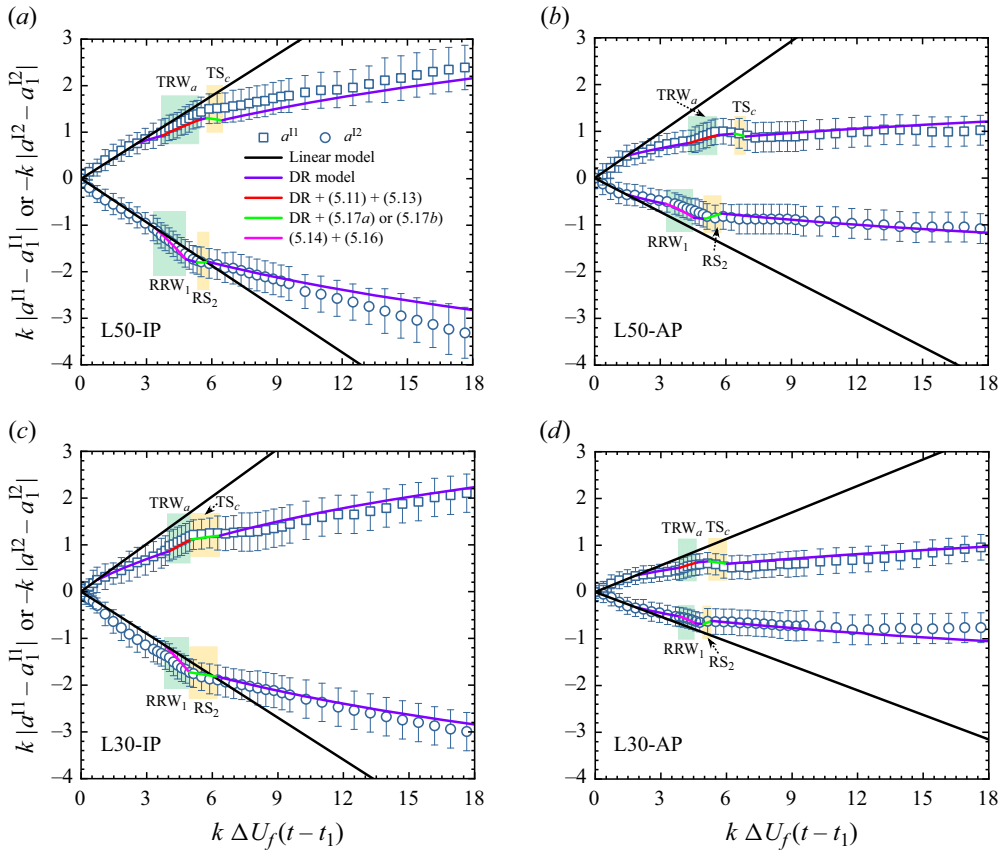
Figure 13. Comparison of the interface amplitude growths between experimental results and theoretical predictions in cases (*a*) L50-IP, (*b*) L50-AP, (*c*) L30-IP and (*d*) L30-AP. The durations of interactions of RRW_1, TRW_a, RS_2 and TS_c with the interfaces are highlighted within the shaded areas.

values of v_t^{I1} and v_t^{I2} given by the linear model (5.7*a*)–(5.7*b*) are in good agreement with the experimental values of v_e^{I1} and v_e^{I2}. The deviation observed in several cases with smaller L_0 values is primarily because SBC and SSC occur early, violating the model's requirement for the non-contact coupling between the two interfaces.

5.2. *Nonlinear amplitude growth*

The collision between fingers directly influences the perturbation growth of both interfaces, resulting in intense nonlinearity. In this subsection, theoretical modelling is conducted to evaluate the nonlinear amplitude growth under finger collision conditions.

5.2.1. *Larger L_0 cases*

First, the nonlinear amplitude growth for the larger L_0 cases is estimated theoretically. Figures 13(*a*)–13(*d*) show the dimensionless amplitude growth for I1 and I2 in cases L50-IP, L50-AP, L30-IP and L30-AP, respectively. It is observed that the nonlinear amplitude growth exhibits an overall logarithmic trend, similar to observations in scenarios of the single interface RMI (Jacobs & Krivets 2005; Morgan *et al.* 2012; Liu *et al.* 2018; Mansoor *et al.* 2020). This implies that the overall logarithmic growth trend during finger

collisions may be described by the nonlinear model proposed for the single interface configuration. Noteworthy are the oscillations in amplitude growth, depicted by shaded areas in figure 13, originating from the interactions of RRW_1, TRW_a, RS_2 and TS_c with the interfaces. These oscillations can be characterized by quantifying the effects of the waves. Subsequently, by superimposing these wave effects onto a suitable nonlinear model, comprehensive estimations of the entire oscillatory nonlinear growth can be obtained.

The nonlinear model (DR model) proposed by Dimonte & Ramaprabhu (2010), applicable to scenarios with various initial interface amplitudes and density ratios, is employed to describe the overall logarithmic nonlinear growth. The DR model expresses the bubble and spike amplitude growth rates ($v_{bu/sp}^{I1}$ and $v_{bu/sp}^{I2}$) for I1 and I2 as follows:

$$v_{bu/sp}^{I1} = \frac{v_{st}^{I1}\left[1 + (1 \mp A_1^*)k\left|v_{st}^{I1}\right|t\right]}{1 + C_{bu/sp}^{I1}k\left|v_{st}^{I1}\right|t + (1 \mp A_1^*)F_{bu/sp}^{I1}\left(k\left|v_{st}^{I1}\right|t\right)^2}, \qquad (5.8a)$$

$$v_{bu/sp}^{I2} = \frac{v_{st}^{I2}\left[1 + (1 \mp A_2^*)k\left|v_{st}^{I2}\right|t\right]}{1 + C_{bu/sp}^{I2}k\left|v_{st}^{I2}\right|t + (1 \mp A_2^*)F_{bu/sp}^{I2}\left(k\left|v_{st}^{I2}\right|t\right)^2}, \qquad (5.8b)$$

where

$$C_{bu/sp}^{I1} = \frac{4.5 \pm A_1^* + (2 \mp A_1^*)k\left|a_{st}^{I1}\right|}{4}, \qquad (5.9a)$$

$$C_{bu/sp}^{I2} = \frac{4.5 \pm A_2^* + (2 \mp A_2^*)k\left|a_{st}^{I2}\right|}{4}, \qquad (5.9b)$$

$$A_1^* = (R_1 - 1)/(R_1 + 1), \qquad (5.9c)$$

$$A_2^* = (R_2 - 1)/(R_2 + 1), \qquad (5.9d)$$

$$F_{bu/sp}^{I1} = 1 \pm A_1^*, \qquad (5.9e)$$

$$F_{bu/sp}^{I2} = 1 \pm A_2^*. \qquad (5.9f)$$

The subscripts '*bu*' and '*sp*' denote bubbles and spikes, and v_{st}^{I1} and v_{st}^{I2} denote the start-up growth rates of the DR model for I1 and I2, respectively, which correspond to v_t^{I1} and v_t^{I2} obtained from the linear model (5.7a)–(5.7b). Also, a_{st}^{I1} and a_{st}^{I2} denote the amplitudes for I1 and I2 at the end of the linear growth.

As discussed in § 4.3, the impacts of TRW_a on the I1 development consist of both RTS and the stretching effect. Here, the Rayleigh model (Rayleigh 1883; Taylor 1950; Mikaelian 2009) is adapted to predict the amplitude growth rate induced by RTS. To simplify the analysis, we assume that the RTS is induced by the 1-D TRW_a, allowing us to substitute the I1 acceleration g_{TRWa}^{I1} into the Rayleigh model, thereby resulting in the modified form

$$\frac{\mathrm{d}v^{I1}}{\mathrm{d}t} = kA_1^* a^{I1} g_{TRWa}^{I1}. \qquad (5.10)$$

Considering the initial conditions $(\mathrm{d}a^{I1}/\mathrm{d}t)|_{t=0} = 0$ and $a^{I1}|_{t=0} = a_{hTRWa}^{I1}$, where a_{hTRWa}^{I1} is the I1 amplitude when the head of TRW_a meets it, and integrating the time term in

Case	L50-IP	L30-IP	L50-AP	L30-AP
Δa_{RTS}^{I1} (mm)	-0.25	-0.09	-0.17	-0.06
$\Delta a_{stretch}^{I1}$ (mm)	1.15	0.75	0.90	0.52

Table 6. Comparison of the amplitude variations (Δa_{RTS}^{I1} and $\Delta a_{stretch}^{I1}$) of I1 resulting from the RTS and the stretching effect.

(5.10), we can obtain the interface amplitude induced by RTS:

$$a_{RTS}^{I1} = \frac{a_{hTRWa}^{I1}}{2} \left(e^{\theta t} + e^{-\theta t} \right), \tag{5.11}$$

where

$$\theta = \sqrt{kA_1^* g_{TRWa}^{I1}}. \tag{5.12}$$

The increase in amplitude ($\Delta a_{stretch}^{I1}$) of I1 due to the stretching effect of TRW_a can be expressed as

$$\Delta a_{stretch}^{I1} = \Delta U_{TRWa}^{I1} \frac{a_{hTRWa}^{I1}}{c_2^*}, \tag{5.13}$$

where c_2^* represents the sound speed at the head of TRW_a.

Table 6 compares the amplitude variations (Δa_{RTS}^{I1} and $\Delta a_{stretch}^{I1}$) of I1 resulting from RTS and the stretching effect. It is observed that the amplitude reduction (Δa_{RTS}^{I1}) caused by RTS is smaller than the increase ($\Delta a_{stretch}^{I1}$) caused by the stretching effect. Consequently, the stretching effect predominates over RTS in influencing I1, thereby enhancing the amplitude growth rate during the TRW_a–I1 interaction, as illustrated in figure 13.

The impacts of RRW_1 on the I2 evolution consist of RTI and the stretching effect. To predict the amplitude growth rate induced by RTI, we modify the ZG model (Zhang & Guo 2016), which characterizes the growth rates of bubbles and spikes at any density ratio. Similar to the approach used for RTS, we consider that the RTI of I2 is induced by the 1-D RRW_1. Then substituting the I2 acceleration g_{RRW1}^{I2} into the ZG model results in the modified form

$$\frac{dv_{bu/sp}^{I2}}{dt} = -\alpha_{bu/sp} k[(v_{bu/sp}^{I2})^2 - (v_{bu/sp}^q)^2], \tag{5.14}$$

where

$$v_{bu/sp}^q = \left(\frac{A_2^* g_{RRW1}^{I2}}{3k} \frac{8}{(1+A_2^*)(3+A_2^*)} \frac{[3+A_2^*+\sqrt{2(1+A_2^*)}]^2}{4(3+A_2^*)+\sqrt{2(1+A_2^*)}(9+A_2^*)} \right)^{1/2}, \tag{5.15a}$$

$$\alpha_{bu/sp} = \frac{3}{4} \frac{(1+A_2^*)(3+A_2^*)}{3+A_2^*+\sqrt{2}(1+A_2^*)^{1/2}} \frac{[4(3+A_2^*)+\sqrt{2}(9+A_2^*)(1+A_2^*)^{1/2}]}{(3+A_2^*)^2+2\sqrt{2}(3-A_2^*)(1+A_2^*)^{1/2}}. \tag{5.15b}$$

The amplitude increment ($\Delta a_{stretch}^{I2}$) of I2 caused by the stretching effect of RRW_1 can be expressed as

$$\Delta a_{stretch}^{I2} = \Delta U_{RRW1}^{I2} \frac{a_{hRRW1}^{I2}}{c_3^*}, \tag{5.16}$$

where a_{hRRW1}^{I2} is the I2 amplitude when the head of RRW_1 just contacts it, and c_3^* is the sound speed at the RRW_1 head.

The impingements of TS_c and RS_2 on I1 and I2 lead primarily to amplitude compressions, denoted as Δa_{TSc}^{I1} and Δa_{RS2}^{I2}, respectively. These reductions in amplitude can be calculated using the expressions

$$\Delta a_{TSc}^{I1} = a_{TSc}^{I1} \frac{\Delta U_{TSc}^{I1}}{V_{TSc}}, \tag{5.17a}$$

$$\Delta a_{RS2}^{I2} = a_{RS2}^{I2} \frac{\Delta U_{RS2}^{I2}}{V_{RS2}}, \tag{5.17b}$$

where a_{TSc}^{I1} (a_{RS2}^{I2}) denotes the amplitude for I1 (I2) when TS_c (RS_2) just contacts it.

The theoretical predictions of the nonlinear growth in the larger L_0 cases are presented in figure 13. The DR model effectively captures the logarithmic nonlinear amplitude growth for both I1 and I2. Equations (5.11) and (5.13) well quantify the amplitude variations resulting from RTS and the stretching effect of TRW_a, and (5.14) and (5.16) well predict the amplitude enhancements resulting from RTI and the stretching effect of RRW_1. Equations (5.17a) and (5.17b) give good predictions of the amplitude compressions caused by TS_c interacting with I1, and RS_2 interacting with I2, respectively. Notably, the SSC results in stagnation of the spike growth (i.e. $v_{sp}^{I1} = 0$, $v_{sp}^{I2} = 0$) for cases L50-AP and L30-AP. To capture the perturbation growth when the spike growth rates approach zero, only the bubble components (v_{bu}^{I1} and v_{bu}^{I2}) of the DR model are adopted. Additionally, the DR model is not included in the prediction during the passage of RRW_1. This is because when using (5.14), the RMI growth rates $v_{bu/sp}^{I2}$ are utilized as initial conditions for integration to obtain the growth rate of RTI induced by RRW_1, implying that (5.14) inherently includes the growth rate induced by RMI.

5.2.2. *Smaller L_0 cases*

The nonlinear amplitude growth for the smaller L_0 cases is estimated theoretically. The interface amplitude growth data in cases L10-IP, L10-AP, L5-IP and L5-AP are plotted in figures 14(a)–14(d), respectively. Since TS_c (RS_2) closely follows the impact of TRW_a (RRW_1) on I1 (I2), counteracting the influence of TRW_a (RRW_1), both I1 and I2 exhibit a smooth logarithmic growth trend in amplitude. Therefore, only the DR model is utilized to predict the nonlinear amplitude growth in these cases. Notably, owing to the limitations of the linear model in accurately capturing amplitude growth rates under certain scenarios (see table 5 for details), the linear growth rate obtained through linear fitting (denoted by dash-dotted lines in figure 14) is employed as the start-up growth rate for the DR model. Remarkably, the DR model provides good predictions of the nonlinear amplitude growth rates for both I1 and I2 in cases L10-IP, L10-AP, L5-IP and L5-AP.

Notably, for cases L10-AP and L5-AP, the abnormal RMI leads to the formation of two bubble structures within a single wavelength at I2, as presented in the schlieren image inset in figure 14(b). The widths of these bubbles, denoted as $h_{bu1} = x_1 - x_3$ and $h_{bu2} = x_2 - x_3$, respectively, are measured from the downstream positions of the bubbles
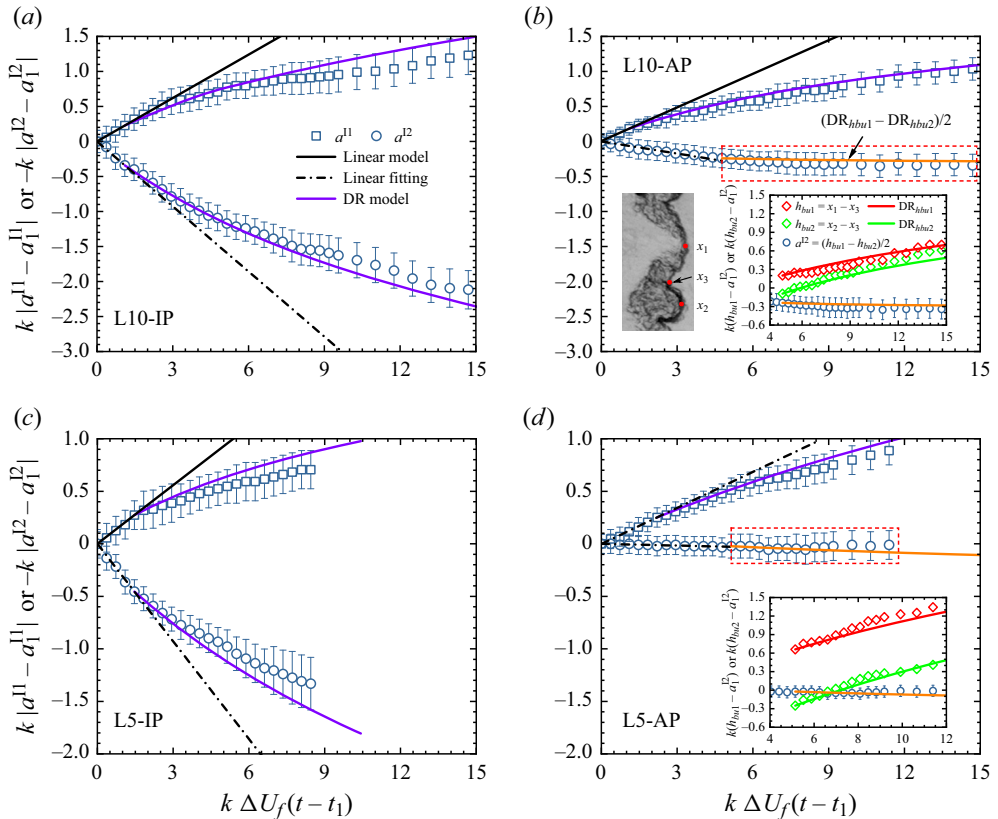
Figure 14. Comparison of the interface amplitude growths between experimental results and theoretical predictions in cases (*a*) L10-IP, (*b*) L10-AP, (*c*) L5-IP and (*d*) L5-AP. Panel (*b*) includes a schlieren image illustrating the abnormal RMI phenomenon at I2, with further details provided in figures 8(*c*) and 8(*d*). The insets in (*b,d*) illustrate the prediction process for the nonlinear amplitude growth of I2 in cases L10-AP and L5-AP. Here, DR$_{hbu1}$ and DR$_{hbu2}$, corresponding to the bubble components of the DR model, are used to estimate the nonlinear amplitude growths for the bubble widths h_{bu1} and h_{bu2}, and (DR$_{hbu1}$ − DR$_{hbu2}$)/2 is used to predict the nonlinear amplitude growth of I2 after the occurrence of the abnormal RMI.

(x_1 and x_2) to their upstream position (x_3). The I2 amplitude (a^{I2}) in the nonlinear growth period can be determined as half the difference between h_{bu1} and h_{bu2}. To predict the nonlinear amplitude growth of I2, h_{bu1} and h_{bu2} are first estimated using the bubble components (DR$_{hbu1}$ and DR$_{hbu2}$) of the DR model. As illustrated in the insets of figures 14(*b*) and 14(*d*), the theoretical predictions represented by the red and green lines for DR$_{hbu1}$ and DR$_{hbu2}$ align well with the experimental results. Then, by computing (DR$_{hbu1}$ − DR$_{hbu2}$)/2, the theoretical prediction, denoted by orange lines in figures 14(*b*) and 14(*d*), effectively captures the I2 nonlinear amplitude growth in both cases L10-AP and L5-AP.

In short, the successful application of the DR model indicates that the nonlinear growth pattern during finger collisions shows similarities to that of a single interface configuration. Specifically, in the SSC cases, although spike growth is dramatically suppressed, the amplitude growth of bubbles on both sides of the layer is minimally affected, remaining comparable to that in a single interface scenario. In the SBC cases, the spike growth of I1 (I2) is inhibited, while the bubble growth of I1 (I2) is promoted. This

inhibition and promotion largely cancel each other out, resulting in the overall amplitude growth of I1 and I2 resembling that of a single interface configuration. As a result, the DR model can describe the nonlinear amplitude growth during finger collisions.

6. Conclusions

The finger collisions in an SF_6/air/SF_6 light fluid layer under reshock conditions are investigated both experimentally and theoretically. Using the soap-film technique, four unperturbed fluid layers with varying thicknesses are generated to analyse the wave dynamics and interface motions during finger collisions; and eight perturbed fluid layers with four thicknesses and two interface phase combinations are created to explore the finger collision mechanism as well as the dependence of collisions on initial conditions. Schlieren photography combined with a high-speed video camera is adopted to capture the shocked and reshocked flows.

Experimental studies and theoretical analyses are conducted for the four unperturbed cases. Compared with the singly shocked scenario that involves only shock–interface interactions, the reshocked case exhibits significantly more complex interactions among shocks, rarefactions, interfaces and the reflecting wall. The wave dynamics in the reshocked case is sensitive to the initial layer thickness. To clarify these phenomena, a 1-D theory is applied, effectively quantifying the motions of layer interfaces, shock waves and rarefaction waves.

The initial condition dependence of finger collisions is examined for the eight perturbed cases. After reshock, the initial in-phase and anti-phase cases experience SBCs and SSCs, respectively. A relatively larger layer thickness allows the downstream interface to reverse phase and develop sufficiently by the time of finger collision. Consequently, the impact forces between the fingers are comparable, resulting in a nearly symmetrical development of the mixing zone. Compared with SBC, SSC greatly inhibits the spike development, resulting in significant growth attenuation of amplitudes and mixing widths. For the smaller thickness cases, the downstream interface has not completed phase reversal by the time of collision, causing the fingers at the upstream interface to dominate in SBC or SSC. In particular, the SSC prevents the downstream interface from reversing its phase, giving rise to abnormal RMI. The abnormal RMI reduces the SSC's ability to suppress the perturbation growth. To maximize SSC effectiveness in attenuating growth, the initial layer thickness should be sufficiently large. This ensures that spikes at both interfaces develop adequately, allowing the spikes to fully collide and thereby cancel out their growth.

The effects of rarefaction waves and the second reshock on interface evolution during finger collisions are studied. Rarefaction waves affect the evolution of both interfaces through the Rayleigh–Taylor and stretching effects. Specifically, the Rayleigh–Taylor effect stabilizes the upstream interface while destabilizing the downstream interface, and the stretching effect enhances the amplitudes of both interfaces. Overall, rarefaction waves facilitate the evolution of both interfaces; however, the second reshock exerts an opposing influence. These wave effects are noticeable primarily in cases with larger layer thicknesses, causing oscillations in their nonlinear amplitude growth. Conversely, in cases with smaller thicknesses, the second reshock promptly interacts with the interfaces after the interactions of rarefaction waves, counteracting their influence. Rarefaction waves stretch the fluid layer, increasing the distance between the two interfaces and thereby reducing the intensity of finger collisions. In contrast, the second reshock compresses the layer, enhancing the collision intensity.

Linear and nonlinear models are developed to predict amplitude growth for both interfaces before and after finger collisions. The reshock-induced amplitude growth rate

is first estimated using a modified form of the Jacobs-type model (Jacobs *et al.* 1995; Liang & Luo 2022*a*). Then this growth rate is combined with the pre-reshock growth rate to establish a linear model that effectively describes the whole linear amplitude growth rate. The DR model (Dimonte & Ramaprabhu 2010) provides good predictions of the RMI-induced nonlinear amplitude growth for both interfaces under SBC and SSC conditions. By quantifying both Rayleigh–Taylor and stretching effects induced by rarefaction waves, along with amplitude compression caused by the second reshock, the oscillations in amplitude growth during finger collisions are predicted successfully.

Declaration of interests. The authors report no conflict of interest.

Author ORCIDs.

Ⓘ Xu Guo https://orcid.org/0000-0002-1280-4968;

Ⓘ Ting Si https://orcid.org/0000-0001-9071-8646;

Ⓘ Xisheng Luo https://orcid.org/0000-0002-4303-8290.

REFERENCES

BAI, X., DENG, X. & JIANG, L. 2018 A comparative study of the single-mode Richtmyer–Meshkov instability. *Shock Waves* **28**, 795–813.

BALAKUMAR, B.J., ORLICZ, G.C., RISTORCELLI, J.R., BALASUBRAMANIAN, S., PRESTRIDGE, K.P. & TOMKINS, C.D. 2012 Turbulent mixing in a Richtmyer–Meshkov fluid layer after reshock: velocity and density statistics. *J. Fluid Mech.* **696**, 67–93.

BALAKUMAR, B.J., ORLICZ, G.C., TOMKINS, C.D. & PRESTRIDGE, K.P. 2008*a* Dependence of growth patterns and mixing width on initial conditions in Richtmyer–Meshkov unstable fluid layers. *Phys. Scr.* **132**, 014013.

BALAKUMAR, B.J., ORLICZ, G.C., TOMKINS, C.D. & PRESTRIDGE, K.P. 2008*b* Simultaneous particle-image velocimetry–planar laser-induced fluorescence measurements of Richtmyer–Meshkov instability growth in a gas curtain with and without reshock. *Phys. Fluids* **20**, 124103.

BALASUBRAMANIAN, S., ORLICZ, G.C. & PRESTRIDGE, K.P. 2013 Experimental study of initial condition dependence on turbulent mixing in shock-accelerated Richtmyer–Meshkov fluid layers. *J. Turbul.* **14**, 170–196.

BALASUBRAMANIAN, S., ORLICZ, G.C., PRESTRIDGE, K.P. & BALAKUMAR, B.J. 2012 Experimental study of initial condition dependence on Richtmyer–Meshkov instability in the presence of reshock. *Phys. Fluids* **24**, 034103.

BETTI, R. & HURRICANE, O.A. 2016 Inertial-confinement fusion with lasers. *Nat. Phys.* **12**, 435–448.

BROUILLETTE, M. & STURTEVANT, B. 1993 Experiments on the Richtmyer–Meshkov instability: small-scale perturbations on a plane interface. *Phys. Fluids* A **5**, 916–930.

BROUILLETTE, M. & STURTEVANT, B. 1994 Experiments on the Richtmyer–Meshkov instability: single-scale perturbations on a continuous interface. *J. Fluid Mech.* **263**, 271–292.

BUTTLER, W.T., *et al.* 2012 Unstable Richtmyer–Meshkov growth of solid and liquid metals in vacuum. *J. Fluid Mech.* **703**, 60–84.

CHARAKHCH'YAN, A.A. 2001 Reshocking at the non-linear stage of Richtmyer–Meshkov instability. *Plasma Phys. Control. Fusion* **43**, 1169.

CHENG, B., KWAN, T.J.T., WANG, Y.M., MERRILL, F.E., CERJAN, C.J. & BATHA, S.H. 2015 Analysis of NIF experiments with the minimal energy implosion model. *Phys. Plasmas* **22**, 082704.

CLARK, D.S., *et al.* 2017 Capsule modeling of high foot implosion experiments on the National Ignition Facility. *Plasma Phys. Control. Fusion* **59**, 055006.

COLLINS, B.D. & JACOBS, J.W. 2002 PLIF flow visualization and measurements of the Richtmyer–Meshkov instability of an air/SF$_6$ interface. *J. Fluid Mech.* **464**, 113–136.

CONG, Z., GUO, X., SI, T. & LUO, X. 2022 Experimental and theoretical studies on heavy fluid layers with reshock. *Phys. Fluids* **34**, 104108.

DIMONTE, G. & RAMAPRABHU, P. 2010 Simulations and model of the nonlinear Richtmyer–Meshkov instability. *Phys. Fluids* **22**, 014104.

DIMONTE, G., TERRONES, G., CHERNE, F.J. & RAMAPRABHU, P. 2013 Ejecta source model based on the nonlinear Richtmyer–Meshkov instability. *J. Appl. Phys.* **113**, 024905.

GAO, X., GUO, X., ZHAI, Z. & LUO, X. 2024 Interfacial instabilities driven by co-directional rarefaction and shock waves. *J. Fluid Mech.* **980**, A20.

GONCHAROV, V.N. 2002 Analytical model of nonlinear, single-mode, classical Rayleigh–Taylor instability at arbitrary Atwood numbers. *Phys. Rev. Lett.* **88**, 134502.

GUO, X., CONG, Z., SI, T. & LUO, X. 2022*a* Shock-tube studies of single- and quasi-single-mode perturbation growth in Richtmyer–Meshkov flows with reshock. *J. Fluid Mech.* **941**, A65.

GUO, X., SI, T., ZHAI, Z. & LUO, X. 2022*b* Large-amplitude effects on interface perturbation growth in Richtmyer–Meshkov flows with reshock. *Phys. Fluids* **34**, 082118.

HAN, Z. & YIN, X. 1993 *Shock Dynamics*. Kluwer Academic.

HOLMES, R.L., DIMONTE, G., FRYXELL, B., GITTINGS, M.L., GROVE, J.W., SCHNEIDER, M., SHARP, D.H., VELIKOVICH, A.L., WEAVER, R.P. & ZHANG, Q. 1999 Richtmyer–Meshkov instability growth: experiment, simulation and theory. *J. Fluid Mech.* **389**, 55–79.

JACOBS, J.W., JENKINS, D.G., KLEIN, D.L. & BENJAMIN, R.F. 1995 Nonlinear growth of the shock-accelerated instability of a thin fluid layer. *J. Fluid Mech.* **295**, 23–42.

JACOBS, J.W., KLEIN, D.L., JENKINS, D.G. & BENJAMIN, R.F. 1993 Instability growth patterns of a shock-accelerated thin fluid layer. *Phys. Rev. Lett.* **70**, 583–586.

JACOBS, J.W. & KRIVETS, V.V. 2005 Experiments on the late-time development of single-mode Richtmyer–Meshkov instability. *Phys. Fluids* **17**, 034105.

KURANZ, C.C., PARK, H.-S., HUNTINGTON, C.M., MILES, A.R., REMINGTON, B.A., PLEWA, T., TRANTHAM, M.R., ROBEY, H.F., SHVARTS, D. & SHIMONY, A. 2018 How high energy fluxes may affect Rayleigh–Taylor instability growth in young supernova remnants. *Nat. Commun.* **9**, 1–6.

LI, J., CAO, Q., WANG, H., ZHAI, Z. & LUO, X. 2023 New interface formation method for shock–interface interaction studies. *Exp. Fluids* **64**, 170.

LIANG, Y. & LUO, X. 2021 On shock-induced heavy-fluid-layer evolution. *J. Fluid Mech.* **920**, A13.

LIANG, Y. & LUO, X. 2022*a* On shock-induced evolution of a gas layer with two fast/slow interfaces. *J. Fluid Mech.* **939**, A16.

LIANG, Y. & LUO, X. 2022*b* On shock-induced light-fluid-layer evolution. *J. Fluid Mech.* **933**, A10.

LIANG, Y. & LUO, X. 2023*a* Hydrodynamic instabilities of two successive slow/fast interfaces induced by a weak shock. *J. Fluid Mech.* **955**, A40.

LIANG, Y. & LUO, X. 2023*b* Review on hydrodynamic instabilities of a shocked gas layer. *Sci. China Phys. Mech.* **66**, 104701.

LINDL, J., LANDEN, O., EDWARDS, J., MOSES, E. & TEAM, N. 2014 Review of the National Ignition Campaign 2009–2012. *Phys. Plasmas* **21**, 020501.

LIU, C., ZHANG, Y. & XIAO, Z. 2023 A unified theoretical model for spatiotemporal development of Rayleigh–Taylor and Richtmyer–Meshkov fingers. *J. Fluid Mech.* **954**, A13.

LIU, L., LIANG, Y., DING, J., LIU, N. & LUO, X. 2018 An elaborate experiment on the single-mode Richtmyer–Meshkov instability. *J. Fluid Mech.* **853**, R2.

LUO, X., LIANG, Y., SI, T. & ZHAI, Z. 2019 Effects of non-periodic portions of interface on Richtmyer–Meshkov instability. *J. Fluid Mech.* **861**, 309–327.

MANSOOR, M.M., DALTON, S.M., MARTINEZ, A.A., DESJARDINS, T., CHARONKO, J.J. & PRESTRIDGE, K.P. 2020 The effect of initial conditions on mixing transition of the Richtmyer–Meshkov instability. *J. Fluid Mech.* **904**, A3.

MARIANI, C., VANDERBOOMGAERDE, M., JOURDAN, G., SOUFFLAND, D. & HOUAS, L. 2008 Investigation of the Richtmyer–Meshkov instability with stereolithographed interfaces. *Phys. Rev. Lett.* **100**, 254503.

MESHKOV, E.E. 1969 Instability of the interface of two gases accelerated by a shock wave. *Fluid Dyn.* **4**, 101–104.

MEYER, K.A. & BLEWETT, P.J. 1972 Numerical investigation of the stability of a shock-accelerated interface between two fluids. *Phys. Fluids* **15**, 753–759.

MIKAELIAN, K.O. 1985 Richtmyer–Meshkov instabilities in stratified fluids. *Phys. Rev.* A **31**, 410–419.

MIKAELIAN, K.O. 1995 Rayleigh–Taylor and Richtmyer–Meshkov instabilities in finite-thickness fluid layers. *Phys. Fluids* **7**, 888–890.

MIKAELIAN, K.O. 1996 Numerical simulations of Richtmyer–Meshkov instabilities in finite-thickness fluid layers. *Phys. Fluids* **8**, 1269–1292.

MIKAELIAN, K.O. 1998 Analytic approach to nonlinear Rayleigh–Taylor and Richtmyer–Meshkov instabilities. *Phys. Rev. Lett.* **80**, 508–511.

MIKAELIAN, K.O. 2009 Reshocks, rarefactions, and the generalized Layzer model for hydrodynamic instabilities. *Phys. Fluids* **21**, 024103.

MIKAELIAN, K.O. & OLSON, B.J. 2020 On modeling Richtmyer–Meshkov turbulent mixing widths. *Physica D* **402**, 132243.

MOHAGHAR, M., CARTER, J., MUSCI, B., REILLY, D., MCFARLAND, J. & RANJAN, D. 2017 Evaluation of turbulent mixing transition in a shock-driven variable-density flow. *J. Fluid Mech.* **831**, 779–825.

MOHAGHAR, M., CARTER, J., PATHIKONDA, G. & RANJAN, D. 2019 The transition to turbulence in shock-driven mixing: effects of Mach number and initial conditions. *J. Fluid Mech.* **871**, 595–635.

MONTGOMERY, D.S., *et al.* 2018 Design considerations for indirectly driven double shell capsules. *Phys. Plasmas* **25**, 092706.

MORGAN, R.V., AURE, R., STOCKERO, J.D., GREENOUGH, J.A., CABOT, W., LIKHACHEV, O.A. & JACOBS, J.W. 2012 On the late-time growth of the two-dimensional Richtmyer–Meshkov instabilities in shock tube experiments. *J. Fluid Mech.* **712**, 354–383.

MORGAN, R.V., CABOT, W.H., GREENOUGH, J.A. & JACOBS, J.W. 2018 Rarefaction-driven Rayleigh–Taylor instability. Part 2. Experiments and simulations in the nonlinear regime. *J. Fluid Mech.* **838**, 320–355.

MORGAN, R.V., LIKHACHEV, O.A. & JACOBS, J.W. 2016 Rarefaction-driven Rayleigh–Taylor instability. Part 1. Diffuse-interface linear stability measurements and theory. *J. Fluid Mech.* **791**, 34–60.

ORLICZ, G.C., BALAKUMAR, B.J., TOMKINS, C.D. & PRESTRIDGE, K.P. 2009 A Mach number study of the Richtmyer–Meshkov instability in a varicose, heavy-gas curtain. *Phys. Fluids* **21**, 064102.

ORLICZ, G.C., BALASUBRAMANIAN, S. & PRESTRIDGE, K.P. 2013 Incident shock Mach number effects on Richtmyer–Meshkov mixing in a heavy gas layer. *Phys. Fluids* **25**, 114101.

ORLICZ, G.C., BALASUBRAMANIAN, S., VOROBIEFF, P. & PRESTRIDGE, K.P. 2015 Mixing transition in a shocked variable-density flow. *Phys. Fluids* **27**, 114102.

PAK, A., DIVOL, L., WEBER, C.R., HOPKINS, L.B., CLARK, D.S., DEWALD, E.L., FITTINGHOFF, D.N., GEPPERT-KLEINRATH, V., HOHENBERGER, M., PAPE, S.L., *et al.* 2020 Impact of localized radiative loss on inertial confinement fusion implosions. *Phys. Rev. Lett.* **124**, 145001.

PROBYN, M.G., THORNBER, R.J.R., WILLIAMS, B., DRIKAKIS, D. & YOUNGS, D.L. 2021 2D single-mode Richtmyer–Meshkov instability. *Physica D* **418**, 132827.

RANJAN, D., NIEDERHAUS, J.H.J., OAKLEY, J., ANDERSON, M.H. & BONAZZA, R. 2009 Experimental investigation of shock-induced distortion of a light spherical gas inhomogeneity. In *Shock Waves*, pp. 1175–1180. Springer.

RAYLEIGH, LORD 1883 Investigation of the character of the equilibrium of an incompressible heavy fluid of variable density. *Proc. Lond. Math. Soc.* **14**, 170–177.

REILLY, D., MCFARLAND, J., MOHAGHAR, M. & RANJAN, D. 2015 The effects of initial conditions and circulation deposition on the inclined-interface reshocked Richtmyer–Meshkov instability. *Exp. Fluids* **56**, 168.

RICHTMYER, R.D. 1960 Taylor instability in shock acceleration of compressible fluids. *Commun. Pure Appl. Maths* **13**, 297–319.

SADLER, J.D., POWELL, P.D., SCHALLES, M., LOUIE, C., JACOBS, J.W. & ZHOU, Y. 2024 Simulations of three-layer Richtmyer–Meshkov mixing in a shock tube. *Phys. Fluids* **36**, 014120.

SADOT, O., EREZ, L., ALON, U., ORON, D., LEVIN, L.A., EREZ, G., BEN-DOR, G. & SHVARTS, D. 1998 Study of nonlinear evolution of single-mode and two-bubble interaction under Richtmyer–Meshkov instability. *Phys. Rev. Lett.* **80**, 1654–1657.

SCHALLES, M., LOUIE, C., PEABODY, K., SADLER, J., ZHOU, Y. & JACOBS, J. 2024 Shock tube experiments on the three-layer Richtmyer–Meshkov instability. *Phys. Fluids* **36**, 014126.

TAYLOR, G.I. 1950 The instability of liquid surfaces when accelerated in a direction perpendicular to their planes. I. *Proc. R. Soc. Lond.* A **201**, 192–196.

URZAY, J. 2018 Supersonic combustion in air-breathing propulsion systems for hypersonic flight. *Annu. Rev. Fluid Mech.* **50**, 593–627.

WANG, H., WANG, H., ZHAI, Z. & LUO, X. 2022 Effects of obstacles on shock-induced perturbation growth. *Phys. Fluids* **34**, 086112.

ZHANG, Q. 1998 Analytical solutions of Layzer-type approach to unstable interfacial fluid mixing. *Phys. Rev. Lett.* **81**, 3391.

ZHANG, Q. & GUO, W. 2016 Universality of finger growth in two-dimensional Rayleigh–Taylor and Richtmyer–Meshkov instabilities with all density ratios. *J. Fluid Mech.* **786**, 47–61.

ZHANG, Q. & GUO, W. 2022 Quantitative theory for spikes and bubbles in the Richtmyer–Meshkov instability at arbitrary density ratios. *Phys. Rev. Fluids* **7**, 093904.

ZHANG, Y., ZHOU, Z., DING, J. & LUO, X. 2022 Interaction of a planar shock wave with two heavy/light interfaces. *Acta Mechanica Sin.* **38**, 322047.

ZHOU, Y. 2017*a* Rayleigh–Taylor and Richtmyer–Meshkov instability induced flow, turbulence, and mixing. I. *Phys. Rep.* **720–722**, 1–136.

ZHOU, Y. 2017*b* Rayleigh–Taylor and Richtmyer–Meshkov instability induced flow, turbulence, and mixing. II. *Phys. Rep.* **723–725**, 1–160.

ZHOU, Y., CLARK, T.T., CLARK, D.S., GLENDINNING, S.G., SKINNER, M.A., HUNTINGTON, C.M., HURRICANE, O.A., DIMITS, A.M. & REMINGTON, B.A. 2019 Turbulent mixing and transition criteria of flows induced by hydrodynamic instabilities. *Phys. Plasmas* **26**, 080901.

ZHOU, Y., *et al.* 2021 Rayleigh–Taylor and Richtmyer–Meshkov instabilities: a journey through scales. *Physica D* **423**, 132838.

ZUCKER, R.D. & BIBLARZ, O. 2019 *Fundamentals of Gas Dynamics*. Wiley.